Cosmochemistry of the Biogenic Elements C, H, N, O, and S

Bruce Fegley, Jr. and Laura Schaefer

Planetary Chemistry Laboratory, Department of Earth and Planetary Sciences

Washington University

St. Louis, MO 63130-4899

Phone: (314) 935-4852

FAX: (314) 935 -7361

bfegley@wustl.edu

laura_s@wustl.edu

Table of Contents

1. Introduction

We discuss the cosmochemistry of the naturally occurring elements with a focus on the biogenic elements carbon, hydrogen, nitrogen, oxygen, and sulfur in this chapter. Broadly speaking, cosmochemistry is the chemistry of the cosmos. This is a very large subject area, which ranges from the nucleosynthesis of elements in stars to their chemistry on the Earth today. We restrict our discussion to chemistry in the solar nebula from which the Sun, Earth, Moon and all other objects in the solar system formed. We describe the cosmochemistry of the biogenic elements as part of a discussion of the cosmochemistry of all naturally occurring elements. This approach shows how the chemistry of other elements affects that of the biogenic elements. This chapter is organized as follows.

We discuss the abundances of elements in the solar nebula in section 2. The solar nebula is the parental material from which the Sun (99.9% of the total mass of the solar system) and the rest of the solar system formed. Thus, elemental abundances in the solar nebula are the solar elemental abundances because they are the elemental abundances in the Sun at the time of its formation. Some nuclides such as deuterium, Li, B, Be are destroyed by thermonuclear fusion in the Sun and their present day abundances are smaller than their initial abundances in the solar nebula. Likewise, the abundances of some radioactive nuclides are lower now than in the solar nebula 4.59 billion years ago. We tabulate the best values for solar elemental abundances for all naturally occurring elements and give the past and present abundances of important radioactive elements.

Section 3 reviews some basic information about the evolution and thermal structure of the solar nebula. The solar nebula formed from a collapsing molecular cloud.

A molecular cloud is a part of interstellar space with higher than average density (100 – 1000 particles cm^{-3} versus ~ 1 particle cm^{-3} in interstellar space) and that contains H_2, CO, and other molecules, instead of only the atomic and ionized H found in interstellar space. We briefly review different models for temperature and pressure as a function of radial distance in the solar nebula because these parameters are critically important for chemistry in the solar nebula.

Section 4 discusses processing of the presolar gas and grains that are the feedstock for the solar nebula. Thermochemical reactions destroyed most of these materials but preservation of isotopic anomalies and presolar grains in meteorites shows that destruction of presolar materials was not 100% efficient. Several of the C-bearing presolar materials that occur in meteorites are diamonds, graphite, silicon carbide, and at least some of the organic material. (However not all of the diamonds, graphite, and organic material are presolar. For example, impacts produced the diamonds in the Canyon Diablo iron meteorite and in the C-rich ureilite meteorites.) We review destruction reactions and preservation sites for some presolar materials in two tables.

Section 5 describes thermochemical equilibrium, or condensation calculations. These are important because heat was the dominant energy source in the solar nebula and drove most of the chemical reactions. Heat was the dominant energy source because the gravitational potential energy of the materials accreted onto the solar nebula was converted into heat. The relatively high mass density of the solar nebula, compared to surrounding interstellar space, diminished the importance of competing energy sources such as UV light, X-rays, and radioactivity. We use sulfur, an important biogenic

element, to illustrate condensation calculations for a major element. We also discuss calculations for minor and trace elements that dissolve in solid solution in phases that are more abundant. Solid solution formation is also important for dissolution of carbon and nitrogen in Fe metal alloy in the solar nebula.

Section 6 summarizes the chemistry of the elements in the solar nebula. Several figures show condensation curves over wide P, T ranges and along a model P, T profile for the solar nebula or along a low-pressure isobar appropriate for the solar nebula. We use the cosmochemical classification of the elements according to volatility to discuss their nebular chemistry. We describe the chemistry of phosphorus, water, and the low temperature ices of carbon and nitrogen in some detail in this section. (The chemistry of sulfur was discussed earlier in section 5.) A table summarizes nebular chemistry of all naturally occurring elements and lists their initial and 50% condensation temperatures, major gases and condensates. This is important because it shows the materials expected in solid grains as a function of temperature (and thus radial distance) in the solar nebula.

Section 7 describes cosmochemistry of carbon and nitrogen and focuses on chemical equilibrium calculations for these two important biogenic elements. The equilibrium gas phase chemistry of carbon shows that CO is the major C-bearing gas at high temperatures and low pressures while CH_4 is the major C-bearing gas at low temperatures and high pressures. The low temperature condensation of these gases was discussed in section 6. The equilibrium gas phase chemistry of nitrogen shows that N_2 is the major N-bearing gas at high temperatures and low pressures while NH_3 is the major N-bearing gas at low temperatures and high pressures. Small amounts of carbon and

nitrogen dissolve in Fe metal alloy because of chemical reactions between CO (or CH_4) and N_2 (or NH_3) with metal grains. Carbide minerals such as cohenite Fe_3C and nitride minerals such as osbornite TiN, and sinoite Si_2N_2O also form via high temperature chemical equilibria under very reducing conditions in some regions of the solar nebula. However, in general much of the carbon in carbonaceous chondrites and in the low metamorphic grade unequilibrated ordinary chondrites is present as organic matter, which does not form at chemical equilibrium.

Section 8 describes grain catalyzed conversion of CO to CH_4 and other hydrocarbons via Fischer-Tropsch type reactions in the solar nebula. Theoretical models predict that a small fraction (≤ 10%) of CO is converted into organic compounds by these reactions. Experimental studies show that CH_4, light hydrocarbons, and polymeric organic material form by metal catalyzed reaction of H_2 plus CO.

Section 9 presents information on the carbon and nitrogen contents of meteorites and the types of C-bearing and N-bearing compounds found in meteorites. This discussion focuses on the chondritic meteorites, which are similar to the materials accreted by Earth during its formation. The three major classes of chondrites (carbonaceous, enstatite, and ordinary) are covered.

2. Elemental Abundances in the Solar Nebula

The solar nebula is the cloud of gas and dust from which the Sun, the Earth, and the other bodies in the solar system formed. A discussion of the cosmochemistry of the biogenic elements requires a working knowledge of solar system elemental abundances (also called solar elemental abundances in this chapter). It is also important to understand how

the solar abundances of the chemical elements have been determined. As we see below, chondritic meteorites, which are stony meteorites that originally formed in the solar nebula, provide much of the abundance data.

During the 19th century, the discovery of new chemical elements, development of the periodic table, and attempts to determine elemental abundances proceeded hand in hand. Chapter 1 of Lodders and Fegley [1] reviews this history in some detail. The American chemist Frank Wigglesworth Clarke (1847 – 1931), who was one of the founders of modern geochemistry, determined elemental abundances in Earth's crust by averaging thousands of chemical analyses of different types of crustal rocks. Clarke also attempted to use the crustal abundances to determine the abundances of the elements in the solar system. However, we now know that the relative elemental abundances in the terrestrial crust are not generally representative of the abundances of rock-forming elements in the solar system. The planetary differentiation, which formed Earth's metallic core, Mg_2SiO_4 (forsterite)-rich mantle, and SiO_2 (silica)-rich crust, redistributed elements between core, mantle, and crust. Consequently, Earth's crustal abundances are different from solar elemental abundances of rock-forming elements.

In order to determine the abundances of elements in the solar nebula, the most useful method is to analyze samples of material that formed therein and that have remained essentially unaltered since that time. The Sun is the single largest reservoir of material from the solar nebula, so one approach has been to spectroscopically determine the elemental abundances in the Sun. The great American astronomer Henry Norris Russell (1877 – 1957) published the first comprehensive table of solar elemental

abundances in 1929. Spectroscopic analysis of the Sun is very useful in some cases. An element must have observable spectroscopic lines, interferences from the lines of other elements are absent or correctable, and the oscillator strengths and transition probabilities for the spectral lines of interest are well known. In addition, it is essential to have realistic physical models of the conditions in the line-forming region of the solar photosphere. At present, solar photospheric abundances are determined for 56 of the 83 naturally occurring elements (e.g., the abundances of carbon, oxygen, and nitrogen) [2]. In some cases, elemental abundances such as those for C, N, O cannot be determined from geochemical analyses of meteorites because meteorites retain only small fractions of the total solar abundances. For example, CI carbonaceous chondrites contain the most carbon of any meteorite, yet their average carbon content of ~ 3.5% corresponds to only 11% of the total carbon abundance in solar material. Neither solar spectroscopy nor geochemical analyses of meteorites provide the solar elemental abundances of the noble gases (He, Ne, Ar, Kr, Xe), which must be determined by other means, as discussed by Lodders [2,3]. In some cases (deuterium, Li, B, Be) thermonuclear fusion has partially or totally consumed an element in the Sun. In other cases, it is impossible to observe spectroscopic lines of an element free from the interference of other elements. In still other cases, the oscillator strengths or transition probabilities of spectral lines are unknown or only poorly known. Lodders [2,3] reviews solar photospheric abundances and compares them with results from meteorites, which we discuss next.

Chondritic meteorites, which have been minimally altered since their formation, are another source of material from the solar nebula. Chondrites are the most abundant

type of meteorites, which are divided into three main classes – stones, irons, and stony irons. The chondrites are stony meteorites, which contain metal, silicate, and sulfide and are so named because they contain small, rounded glass beads known as chondrules. The chondrites are unmelted stony meteorites, which are the oldest objects in the solar system. Chemical and isotopic data indicate that the chondrites formed in the solar nebula and were relatively unaltered (compared to other types of meteorites) since that time.

The three major types of chondrites are carbonaceous chondrites (e.g., CI, CM, CV, CO, CK), ordinary chondrites (H, L, LL), and enstatite chondrites (EH, EL). The carbonaceous chondrites are of most interest to us for two reasons. First, the elemental abundances of rock-forming elements in CI chondrites are the same as those in the Sun. Second, the CI and CM carbonaceous chondrites contain large amounts of carbon and organic material. The Orgueil meteorite is the largest and thus most analyzed CI chondrite. The Murchison meteorite is the largest and most analyzed CM chondrite.

The achondrites, which comprise the rest of the stony meteorites, were melted at some point in time, presumably in the silicate portion of their meteorite parent bodies. The stony iron and iron meteorites were also melted at some point in time, presumably at the silicate – iron boundary and inside the iron core of meteorite parent bodies. Thus, the elemental abundances in the achondrites, stony iron, and iron meteorites were altered by planetary differentiation, and are different than the solar elemental abundances.

The pioneering Norwegian geochemist Victor M. Goldschmidt (1888 – 1947) and his colleagues Ida (1896 – 1978) and Walter (1893 – 1960) Noddacks did extensive chemical analyses of stony and iron meteorites and terrestrial rocks. Goldschmidt [4,5]

compiled the first comprehensive table comparing elemental abundances in meteorites, the Sun, and the Earth's crust which showed that, to first approximation, the abundances of the rock-forming elements in chondrites and in the Sun were similar.

Goldschmidt also developed the geochemical classification of the elements, which is widely used today. Atmophile elements are mainly found in the Earth's atmosphere (e.g., N, O, He, Ne, Ar, Kr, Xe). Biophile (or biogenic) elements are concentrated in living organisms (e.g., H, O, C, N, P). Chalcophile elements prefer to be in sulfides (Fe, Pb, S, Se, Mo, W). Hydrophile elements are soluble in water (e.g., B, F, Cl, Pb). Lithophile elements are found in rocks (e.g., B, Al, Ca, K, Mg, Si, O, P). Siderophile elements are preferentially found in metal (Fe, Ni, Ir, Pd, Pt, Os, Ru). Several elements occur in two or more groups because their geochemical affinity changes depending on environmental conditions such as the temperature and partial pressure of oxygen. (The partial pressure of oxygen and the oxygen fugacity are identical for an ideal gas and we use them synonymously throughout this chapter.)

Goldschmidt's work on elemental abundances stimulated research on elemental abundances in meteorites and the synthesis of elements in stars by other scientists, notably the American chemists Harrison Brown (1917 – 1986), Harold Urey (1893 – 1981), and the Austrian chemist Hans Suess (1909 – 1993). Suess [6,7] proposed that the abundances of the nuclides, and especially the odd mass number nuclides, are a smooth function of mass number. He used this postulate to adjust the elemental abundances to produce a smooth variation of abundance with mass number. In some cases, such as Re, adjustments of up to a factor of 100 were made. Subsequently, chemical analyses of

meteorites (e.g., [8]) showed that Suess' adjustments were correct. Brown [9] also published a revised table of elemental abundances that improved upon Goldschmidt's work in several respects.

Several years later Suess and Urey [10] carried this approach even further and produced an influential table of solar elemental abundances. Their table led to pioneering studies of stellar nucleosynthesis mechanisms by Burbidge et al. [11] and Cameron [12]. The Suess and Urey paper also led to an increasing number of high quality analytical studies of elemental abundances in chondritic meteorites. Much of this work is summarized in two compilations edited by Mason [13,14]. The papers by Anders and Ebihara [15], Anders and Grevesse [16], Cameron [17], and Lodders [2] review more recent work on elemental analyses of meteorites. In the over 50 years since the publication of Suess and Urey [10], the improvements in chemical analyses of meteorites, in the understanding of stellar nucleosynthesis mechanisms, and in astronomical observations of elemental abundances in the Sun and other stars have led to vast improvements in our knowledge of the solar abundances of the elements.

The result of all these efforts is displayed in Table 1, based on Lodders [2,3], which summarizes present knowledge of the solar abundances of the elements. It shows the protosolar atomic abundances of the elements (normalized to 10^6 atoms of Si). The protosolar abundances are those in the solar nebula during formation of the solar system. The protosolar abundances are slightly different than elemental abundances in the solar photosphere because of heavy element settling in the Sun [2].

Perhaps the single most important point illustrated by the data in Table 1 is that the chemistry of solar composition material and of the solar nebula is overwhelmingly dominated by hydrogen. Helium, which is non-reactive, is the second most abundant element. The third most abundant element overall and the second most abundant chemically reactive element, oxygen, has only about 0.1% of the H atomic abundance in solar matter. Table 1 also shows that the abundances of all other elements (other than H and He) are less than that of oxygen.

The dominance of hydrogen controls the chemistry of solar composition material, which resembles that of the atmosphere of Jupiter to first approximation. Water vapor, CH_4 (at low temperatures), NH_3 (at low temperatures), and H_2S are the major gases for oxygen, carbon, nitrogen, and sulfur. Molecular oxygen is absent and the oxygen fugacity is controlled by chemical equilibria between water vapor and H_2

$$2H_2O = 2H_2 + O_2 \tag{1}$$

$$\log fO_2 = 2\log\left(\frac{X_{H_2O}}{X_{H_2}}\right) + 5.67 - \frac{25{,}664}{T} \tag{2}$$

The mole fractions of water vapor and H_2 are used in Eq. (2). The solar elemental abundances and the chemistry of carbon and oxygen (see below) dictate that the (H_2O/H_2) molar ratio is about 5.8×10^{-4} over a wide range of conditions in the solar nebula, where all carbon is present as CO gas. Equation (2) for the temperature-dependent oxygen fugacity of solar composition material then becomes

$$\log fO_2 = -0.80 - \frac{25{,}664}{T} \tag{3}$$

At 1300 K in the inner solar nebula, Eq. (3) gives an oxygen fugacity of $10^{-20.5}$ bar. This is very reducing compared to the oxygen fugacities of terrestrial rocks and volcanic gases. For example, the oxygen fugacity of volcanic gases erupted at Kilauea in Hawaii at the same temperature is about $10^{-10.2}$ bars (Table 6.3 of [18]). The very low oxygen fugacity of solar composition material means that the solar nebula was chemically reducing and that reduced compounds predominated.

A second important point is that the chemistry of oxygen and carbon, the second and third most abundant chemically reactive elements in the solar system, is intimately coupled due to their very similar atomic abundances (C/O ~ 0.5). Unfortunately, their elemental abundances are notoriously difficult to determine and are somewhat uncertain. Consequently the C/O ratio fluctuates with time from one abundance compilation to another, and has ranged from 0.16 [10] to 0.60 [15]. Most values with the exception of that of Suess and Urey [10] fall into the range of 0.42 – 0.60. The two major C-bearing gases in solar composition material over a wide P, T range are CO and CH_4 [19]. These two gases are converted into one another by the net reaction

$$CO + 3H_2 = CH_4 + H_2O \qquad (4)$$

$$\log K_1 = 11{,}069.94/T - 1.17969 \log T - 8.96596 \qquad (5)$$

Equation (5) gives the equilibrium constant for reaction (4) from 298 – 2500 K. Chemical equilibrium calculations using this data and the solar elemental abundances show that CO is stable at high temperatures and low pressures while CH_4 is stable at low temperatures and high pressures in solar composition material (e.g., see the extensive discussion in [19]). The temperatures and pressures at which CO is stable coincide with

those expected in the inner regions of the solar nebula. In the inner solar nebula, CO is the most abundant carbon gas and is also either the first or second most abundant oxygen gas, depending on the degree of dissociation of water vapor.

Changes in the the bulk C/O ratio in the gas phase, e.g., by vaporization of presolar graphite grains or presolar organic material (see Table 2), or by freezing out water vapor, lead to changes in the gas phase abundance of CO and H_2O. Changes in the C/O ratio also alter the oxygen fugacity of the solar nebula and the major element mineralogy of grains formed from the nebular gas, e.g., [20-22]. The C/O ratio is also important for determining the amount of water ice in volatile-rich bodies that formed in the outer solar nebula.

Thermodynamics predicts that reaction (1) proceeds to the right, i.e. toward methane as temperature decreases. However, the kinetics of the gas phase conversion of CO to CH_4 become so slow that this may not happen [23] unless grain catalyzed reactions occur [24]. If all carbon remained as CO at the low temperatures in the outer nebula, then the water ice abundance was decreased below the amount which could condense if CO were converted to CH_4. On the other hand, if CO were efficiently converted to CH_4 and/or other hydrocarbons, then a sizable fraction of the total O was released from CO and was available for formation of water ice. The water ice/rock mass ratios in "icy" bodies formed in the solar nebula, where CO was the dominant carbon gas, are predicted to be lower than the water ice/rock ratios in "icy" bodies formed in the subnebulae around Jupiter and Saturn, where CH_4 was the dominant carbon gas. (Planetary scientists think that the Galilean satellites (Io, Europa, Ganymede, and Callisto) of Jupiter and Titan and

other regular satellites of Saturn formed in miniature versions of the solar nebula known as subnebulae. These existed around Jupiter and Saturn during their formation and were higher density regions with different chemistry than the surrounding solar nebula.)

Finally, the elemental abundances in Table 1 show that the chemistry of the solar nebula (and of solar composition material) is essentially the chemistry of eight elements (H, O, C, N, Mg, Si, Fe, S). To a lesser extent Al, Ca, Na, Ni, Cr, Co, P, and Mn are also important by virtue of their abundances. Several of these less abundant elements (Ni, Cr, Co) form alloys with Fe or dissolve in other more abundant phases (Mn silicates dissolving in forsterite and enstatite). Thus, to a good first approximation, elemental abundances dictate that the chemistry of solar material is the chemistry of only a handful of the naturally occurring elements.

3. Evolution and Thermal Structure of the Solar Nebula

Now that we have reviewed the elemental abundances in the solar nebula we need to discuss the physical conditions in the solar nebula and how these conditions changed with time. Physical models of the solar nebula are based on astronomical observations of protoplanetary disks and young stars, geochemical analyses and geochronological dating of meteorites, and theoretical modeling of accretion disks. One such model is that of Cameron [25], which divides the evolution of our solar nebula into four stages. We summarize Cameron's (1995) model below.

Stage 1: Molecular cloud collapse. During this stage, infalling material from the collapsing molecular cloud core forms the solar nebula, which is one type of accretion disk. This stage lasts for a few hundred thousand years. The mass of the solar nebula is

greater than the initial proto-solar mass, but most (if not all) of the matter in the nebular disk ultimately goes into the proto-Sun and is not preserved in asteroids, comets, meteorites, planets, or satellites.

Stage 2: Disk dissipation. The Sun forms during this stage, which lasts for about 50,000 years (in other words the Sun accretes at a rate of about 2×10^{-5} solar masses per year). The disk mass is less than the mass of the proto-Sun. Most matter falling onto the accretion disk is transported through the disk into the proto-Sun. Thus, there is a general mass transport inward. However, the amount of outward mass transport, which "contaminates" the outer nebula with products from thermochemical processing in the innermost few AU of the nebula, is controversial and uncertain. There is also an angular momentum transport outward in the geometrically thin disk. Near the end of stage 2, some disk material survived and is preserved in meteorites (e.g., ^{26}Al-bearing minerals). Some materials in comets and in other primitive bodies (Kuiper Belt Objects, Plutoids, outer planet satellites) may date from this stage as well.

Stage 3: Terminal accumulation of the Sun. The final accumulation of the Sun occurs during this stage, which lasts for about one to two million years and the accumulation rate of the Sun decreases from about 10^{-7} to 10^{-8} solar masses per year. The proto-Sun becomes a classical T Tauri star in this phase. (A T Tauri star is a young star shortly after its formation before it enters the main sequence on the Hertzsprung – Russell Diagram.) Planetary accretion, which is almost complete for Jupiter and Saturn, and less advanced for the other planets, also occurs during this stage. Subnebulae form around Jupiter and Saturn during their formation. The higher pressures and temperatures in the

subnebulae lead to thermochemical reactions (e.g., conversion of CO into CH_4, conversion of N_2 into NH_3, Fischer-Tropsch type synthesis of organic compounds from CO and H_2) which may contaminate the outer solar nebula and be accreted into comets and other primitive bodies.

Stage 4: Loss of nebular gas. The Sun becomes a weak line T Tauri star in this stage, which lasts 3 – 30 million years, and is no longer accreting material from the disk. The T Tauri wind removes gas in the inner nebula and photoevaporation due mainly to UV radiation from the T Tauri wind removes gas in the outer nebula. UV photochemistry and ion-molecule chemistry may be important disequilibrating processes in the outer nebula, but depend on the nebular column density, which is poorly constrained and time dependent [25]. Gas-grain chemistry throughout the nebula ceases sometime (although not necessarily at the same time everywhere) during this stage.

In this model of nebular evolution, the accumulation of the Sun consumed essentially all of the material accreted by the nebular disk during the early stages of its history. Planets, meteorites, comets, and the other bodies in the solar system formed from material accreted after the Sun had formed (i.e., from the end of stage 2 into stage 4).

The temperature and pressure in the nebula during its latter history were important for chemical and physical reprocessing of presolar material. Three models of temperature and pressure as a function of radial distance in the solar nebula are contrasted in Figure 1. These three models are derived using different assumptions and differ in detail. However, they all predict low temperatures that agree within a factor of two and pressures that agree within an order of magnitude in the outer solar nebula. None of the models extend

out as far as 1000 AU, the outer edge of the Kuiper Belt, and background values of temperature (~10 K) and pressure (10^3 cm^{-3} number density giving 10-18 bar at 10 K) are assumed there.

In fact, the radial extent of the solar nebula, the lowest temperatures attained in the outer nebula, and how the nebular disk blended into the surroundings are poorly constrained. The presence of N_2, CO, and CH_4 ices on Triton and Pluto, and of CH_4 ice on some Kuiper Belt Objects (e.g., Eris, Quaoar, Sedna) show that temperatures were low enough to condense these ices in the outer solar nebula (i.e., about 25 K for a wide range of plausible pressures). If these bodies formed at or near their present locations then temperatures were ~25 K at 30-40 AU when Triton, Pluto, and CH_4-bearing Kuiper Belt Objects formed. However, temperatures could not drop below background temperature.

Finally, all three models are snapshots at one point in time when the snowline, where water ice condenses, was at Jupiter's orbit (5.2 AU) and the tar line (where polymeric organic matter like that in carbonaceous chondrites forms) was in the asteroid belt. We know this because the Galileo entry probe showed that Jupiter is enriched in carbon, but depleted in oxygen and water relative to solar abundances [26]. Thus, polymeric organic matter like that in carbonaceous chondrites provided the glue for the runaway accretion of rocky material to form Jupiter's core. Observations of asteroids with spectral features due to organic matter and/or water-bearing minerals [27] show that as the nebula cooled the snowline and tar line moved inward to the asteroid belt.

4. Processing of Presolar Gas and Grains in the Solar Nebula

Solar elemental abundances give the average composition of the gas and grains that formed the solar nebula, but they do not tell us how what form(s) each element was in when it was accreted by the solar nebula. As discussed below, this information is potentially important because observations of presolar grains in meteorites show that thermal processing in the solar nebula was not perfectly efficient, or else presolar grains would not be found in meteorites. (We use the term presolar to describe the pre-existing gas and grains that were formed the solar nebula and by definition predate the Sun and other bodies in the solar system.) The preservation of isotopic anomalies in meteorites also shows that thermal processing was not 100% efficient.

Qualitatively we expect that the presolar gas and grains were thermally and chemically reprocessed to varying degrees depending on several factors such as the distance of the accreted material from the proto-Sun, the type of grains (e.g., icy, metallic, organic, rocky, etc.), whether the presolar material was accreted when the nebula was hot or cold, the rate of radial transport in the solar nebula relative to the rate of equilibrating reactions in the gas parcel, and to the rate of accretion of small grains into larger clumps. Obviously some grains in the solar nebula experienced complex histories such as cycles of evaporation, condensation, re-evaporation, and re-condensation. Other grains were presumably totally destroyed while some others were incorporated into meteorite parent bodies essentially unaffected by nebular processes.

A variety of sources provide information on the probable composition of the gases and grains accreted by the solar nebula. In recent years radio astronomy has detected a diverse suite of molecules in interstellar space and in the circumstellar shells of carbon

stars, see e.g. [28-30]. At present about 150 molecules ranging in complexity from OH to $HC_{11}N$ have been detected. Tables 2 (grains) and 3 (gas) schematically summarize a small subset of these data on the composition of interstellar and circumstellar gas and grains, indicate the possible effects of nebular chemistry on the accreted gas and grains, and also list possible preservation sites for the presolar species.

Several important points are indicated by these two tables. Perhaps the most significant is that the identification of presolar material in primitive objects (e.g., comets and some types of asteroids and meteorites) may be ambiguous because several important interstellar molecules are also predicted to form in the solar nebula. This problem may be most severe for CO and N_2. If complete chemical equilibrium were attained, all interstellar carbon species would be converted to CO in the high temperature regions of the solar nebula and all interstellar nitrogen species would be converted to N_2. In the absence of a potentially diagnostic isotopic ratio, it is then impossible to distinguish interstellar CO and N_2 from nebular CO and N_2. Likewise, interstellar H_2S, unless it is isotopically distinctive in some way, is impossible to distinguish from nebular H_2S.

A similar problem exists for distinguishing presolar silicates and oxides from those produced by thermal processing (e.g., condensation, evaporation) in the solar nebula. Again, isotopic differences are one way to distinguish exotic material. Presolar oxides (mainly corundum Al_2O_3 and spinel $MgAl_2O_4$) have been identified by ion probe studies [31-39]). Presolar silicates (pyroxene and olivine) have also been identified using O-isotope imaging with the NanoSIMS by Nguyen and Zinner [40]. If this is not possible, for example by virtue of small sample size which prohibits isotopic measurements, then

other approaches may prove useful. For example, Bernatowicz et al [41] discovered small (7-21 nm) crystals of TiC inside isotopically anomalous graphite grains which are clearly of presolar origin. Thus, the included TiC must also be presolar. Analogously, finding a silicate inside another grain, which by virtue of its mineralogy and/or isotopic composition is clearly presolar, may also be used as proof of a presolar origin. However, because the average composition of the gas and grains accreted by the solar nebula has solar chemical and isotopic composition, by definition, then it is clear that not all presolar material has to be isotopically distinctive from nebular materials. Lodders and Amari [42] give a full review of presolar grains.

However, some presolar grains have distinctive compositions which are not representative of thermal processing in the solar nebula. The SiC, TiC, diamond, and graphite grains found in primitive meteorites (see [42]) are probably the best examples of this situation. As discussed by Fegley [24], SiC, TiC, and diamond are thermodynamically unstable in the solar nebula and would be oxidized to other compounds at the high temperatures in the inner solar nebula. As discussed later, graphite is stable at low pressures and low temperatures in a solar composition gas, but is thermodynamically unstable under all other conditions. But even in these relatively clear cut cases there is still room for some ambiguity. Silicon carbide and graphite are also predicted to be thermodynamically stable under the highly reducing conditions necessary for formation of the enstatite chondrites [20,21]. Diamond is not thermodynamically stable under these conditions but diamonds formed by impacts are also present in the

ureilites, carbon-rich achondrites. Even in these cases, the identification of the SiC, graphite, and diamond grains as presolar rests upon their exotic isotopic compositions.

5. Thermochemical Equilibrium (Condensation) Calculations

Although thermal processing of presolar gas and grains was not perfectly efficient, most of the presolar material was reprocessed in the solar nebula. The abundance of presolar grains in chondritic meteorites is only a few μg/g (SiC, graphite) to a few hundred μg/g (presolar diamonds) (see Table 4 of [42]). These abundances are very small in comparison to the total carbon and silicon abundances in meteorites. The CI carbonaceous chondrites contain the most presolar diamonds (940 – 1400 μg/g) of any meteorite. The total carbon abundance in CI chondrites is 35,180 μg/g [2]. Most of the carbon (~ 70%) is in polymeric organic material, a few percent is in carbonate minerals, and much of the rest is in soluble organic compounds. A tiny fraction of the carbon in CI chondrites is in presolar diamonds, about 2.7 – 4.0%. The CI chondrites also contain 14 μg/g of presolar SiC, versus a total Si abundance of 106,500 μg/g [2,42]. A comparison of the C and Si abundances in presolar grains in other types of chondrites gives similar results, except that even less of the total C and Si are found in presolar grains. Most of the original presolar grains and an unknown fraction of presolar organic material were destroyed in the solar nebula where most of the reprocessing was due to thermally driven reactions, e.g., see [43]. Furthermore, to at least first approximation, chemical equilibrium models (see [44] and references therein) can explain the chemistry and mineralogy of chondritic meteorites. Thus, we next consider thermochemical equilibrium calculations of nebular chemistry, which are known as condensation calculations.

5.1 Computational Methods and Nomenclature

Thermochemical equilibrium, or condensation, calculations predict the distribution of each element between its gaseous, solid, and liquid compounds as a function of temperature, pressure, and bulk composition. The bulk composition is given by the solar elemental abundances (see Table 1). Nebular models, such as those shown in Figure 1, give pressure and temperature. All naturally occurring elements can be included in the calculations and the number of compounds included in the calculations is only limited by the available thermodynamic data. Sophisticated computer codes, such as the CONDOR chemical equilibrium code [45-48], calculate the equilibrium chemistry of all elements simultaneously. This is important because the chemistry (species in the gas, type of condensate) of minor elements is affected by that of major elements. For example the CONDOR code simultaneously solves for mass balance and chemical equilibrium of over 2000 gases and 1600 condensates of all naturally occurring elements. We use sulfur as an example to illustrate condensation calculations of solar nebula chemistry.

Sulfur is the tenth most abundant element in the solar system and the fourteenth most abundant element in the Earth's crust (697 μg/g). Sulfur is critically important for life on Earth and is the sixth most abundant element in the average human body (0.64%), and is the ninth most abundant element in plants (0.07%). Sulfur is more abundant in humans (and other animals) than in plants, because it mainly occurs in proteins and plants contain less protein than animals. Sulfur occurs in structural proteins found in fingernails, fur, and hair. The three S-bearing amino acids are methionine ($H_3CS(CH_2)_2CHNH_2COOH$), cysteine ($HSCH_2CHNH_2COOH$), and cystine ($-SCH_2CHNH_2COOH)_2$. The disulfide

linkages of these amino acids provide three dimensional structure and mechanical strength for the proteins in fingernails, fur, and hair.

The condensation calculations consider mass balance and mass action (chemical equilibrium). We define the total abundance of sulfur in all forms as A(S), which is the atomic abundance of S relative to 10^6 Si atoms. This value is given in Table 1 and is about 444,900 sulfur atoms. The total mole fraction (X) of total sulfur (ΣS) is then

$$X_{\Sigma S} = \frac{A(S)}{A(H + H_2 + He)} \tag{6}$$

where A(H+H_2+He) is the sum of the H and He abundances with the temperature-dependent H and H_2 equilibrium taken into account. In the actual computation, other gases such as CO, H_2O, N_2, Ne, ions, etc., are also included in the denominator, but these are neglected in the description here for clarity. Multiplying $X_{\Sigma S}$ by the total pressure $P_{\rm tot}$ in the solar nebula gives the partial pressure sum for sulfur,

$$P_{\Sigma S} = X_{\Sigma S} P_T = P_S + 2P_{S_2} + P_{HS} + P_{H_2S} + P_{PS} + P_{SiS} + P_{SO} + P_{SO_2} + P_{CS} + P_{OCS} + \ldots \tag{7}$$

Equation (7) is a mass balance equation that counts the total number of sulfur atoms in all S-bearing gases and equates this sum to the total amount of sulfur. You can see that the partial pressures of S-bearing gases with more than one sulfur atom are multiplied by the number of sulfur atoms in the gas to insure that all atoms are counted. We must now relate the partial pressures of the different S-bearing gases in the mass balance equation to their chemical equilibrium abundances.

This is done by rewriting equation (7) in terms of the thermodynamic activity of S (a_S, or equivalently using the square root of the S_2 fugacity), the equilibrium constants

(K_i) for forming the S-bearing gases from the constituent elements in their reference states, and the thermodynamic activities and fugacities of all other elements combined with sulfur in the gases,

$$P_{\Sigma S} = X_{\Sigma S} P_T$$

$$= a_S [K_S + 2K_{S_2} a_S + K_{HS} f_{H_2}^{1/2} + K_{H_2S} f_{H_2} + K_{PS} f_{P_2}^{1/2} + K_{SiS} a_{Si} + K_{SO} f_{O_2}^{1/2} + K_{CS} a_{graphite}$$

$$+ K_{OCS} a_{graphite} f_{O_2}^{1/2} + ...] \qquad (8)$$

The actual mass balance sum for sulfur in the CONDOR code includes over 100 S-bearing gases. The most important ones in a solar composition gas are S, HS, H_2S, and SiS (see Figure 2). Analogous forms of equation (8) are written for each element in the code. The equilibrium constants (K_i) in the equations are taken from thermodynamic data compilations such as the JANAF tables and the primary thermodynamic literature. The a_i and f_i terms in equation (8) are the elemental activities and fugacities of the respective elements, e.g., a_{Si} is the elemental activity of silicon.

Equation (8) combines the mass balance and mass action constraints for sulfur. It also shows that the chemistry of sulfur is coupled to that of other elements because the partial pressures of H_2S, PS, SiS and so on are included in equation (8). In general, the chemistry of all the elements is coupled, and the mass balance equations from the set of coupled, nonlinear equations are solved iteratively. An initial guess is assumed for the activity or fugacity of each element. These guesses can be optimized if the major gas for each element is known, but this is not necessary for the code to operate properly. The CONDOR code solves the set of mass balance equations and returns the thermodynamic activity or fugacity for each element, the abundances of all gases (molecules, radicals,

atoms, ions) included in the code, and information on the quality of the calculated results for each element. The convergence criterion requires that the calculated and input abundances for each element agree to within 1 part in 10^{15}.

Condensate stabilities are computed considering compound formation from the elements in their respective reference states. For example, the reaction

$$\text{Fe (metal)} + \text{S (ref state)} = \text{FeS (troilite)} \tag{9}$$

is used for troilite. The reference state of sulfur is either S_2 (g) or elemental S depending on the temperature. As temperature decreases, reaction (9) shifts to the right and the thermodynamic activity of troilite increases. Troilite condenses when its thermodynamic activity reaches unity and this is calculated from

$$a_{FeS} = a_{Fe} a_S K_{FeS} \tag{10}$$

where K_{FeS} is the temperature-dependent equilibrium constant for troilite, and a_{Fe} and f_{S2} are taken from the gas-phase equilibrium calculations described above. To first approximation, a plot of log a_{FeS} versus inverse temperature is a straight line, similar to the behavior of equilibrium constants. The activities of all other possible condensates are computed in a similar fashion. (The concept of activity is defined in many thermodynamic textbooks, such as [49].) At the temperature at which the thermodynamic activity of a pure phase (e.g., Fe-metal, corundum [Al_2O_3], iron sulfide[FeS]) reaches unity, the compound or element begins to condense from the gas phase. This temperature is the condensation temperature.

Once troilite is stable, the fraction of S (α_S) condensed in troilite is calculated and the gas-phase abundance of total sulfur ($P_{\Sigma S}$) is reduced by multiplying by (1 - α_S) (see

also [50] for this procedure). Analogous corrections are made for all elements distributed between the gas and condensates. The gas-phase and gas-solid chemical equilibria are coupled and solved simultaneously using iterative techniques.

5.2 Results of Condensation Calculations for Sulfur

Figures 2 and 3 illustrate the results of the condensation calculations for sulfur. The computations in Figure 2 were done for the Lewis [51] solar nebula P, T profile shown in Figures 1 and 4. This is an adiabatic P, T profile having T = 600 K and P = 10^{-4} bars at 1 AU radial distance in the solar nebula. An adiabatic profile means that heat is transported by convection and that most of the nebula is opaque to thermal radiation because of absorption and scattering by gases (e.g., H_2O, CO, CH_4, NH_3, H_2S) and grains (e.g., Fe metal, silicates, sulfides, and organic material and ices at low temperatures). Radiative transport of heat only becomes important in the outer skin of the nebula (its photosphere) where it becomes transparent to heat radiation. The results in Figure 2 would only be slightly different if the calculations were done along another thermal profile (e.g., another adiabat, or an isobar) and the qualitatively important features would remain the same. Figure 3 is calculated along the 10^{-4} bar isobar and you can see that the results are slightly different than those in Figure 2 but are qualitatively similar.

At the highest temperatures shown in Figure 2, all sulfur is in the gas phase and the three most abundant S-bearing gases are monatomic sulfur, the HS (mercapto) radical and H_2S. A few percent of sulfur is also present in SiS gas. We mentioned earlier that the mass balance sum for sulfur includes over 100 S-bearing gases. Although all of these gases are present, their thermochemical equilibrium abundances are so small that they

cannot be plotted on Figure 2. For example, at 2200 K, S_2, PS, SO, and OCS - some of the other gases listed in our illustrative mass balance equation for sulfur - comprise about 0.05%, 0.02%, 0.17%, and 3.4×10^{-4}% of total sulfur, respectively. None of these gases is abundant enough to be shown in Figure 2.

Figure 3 shows the abundance of S-bearing gases plotted as log mole fraction versus temperature. This plot stops at 750 K, just above the troilite condensation temperature. It shows that monatomic S is the major sulfur gas at high temperatures, that HS briefly is the major sulfur gas, and that H_2S is the major S-bearing gas over most of the temperature range in the inner solar nebula. In contrast to Figure 2, it also clearly shows the abundances of minor and trace sulfur gases such as SiS, S_2, and PS. On the other hand, Figure 2 gives a better picture of the percentage distribution of sulfur between its major gases and condensates. The other S-bearing gases in the mass balance sum for sulfur are not abundant enough to appear on Figure 3. In general, the abundances of minor and trace gases of an element are important for chemical kinetic models of nebular chemistry. For example, the abundance of formaldehyde H_2CO, a minor C-bearing gas, is important for modeling kinetics of the CO to CH_4 conversion.

Figures 2 and 3 show that monatomic S gas and the HS radical become less abundant while H_2S becomes more abundant with decreasing temperature in the solar nebula. Initially, SiS gas also becomes more abundant with decreasing temperature, but there is an abrupt break in the SiS curve in Figures 2 and 3. This break occurs because condensation of magnesian silicates such as forsterite (Mg_2SiO_4) and enstatite ($MgSiO_3$) depletes Si in the gas and abruptly decreases the SiS gas abundance. Once SiS gas

disappears, H_2S contains virtually 100% of all sulfur and no other S-bearing gases are nearly as important (see Figure 3). The disappearance of SiS gas coincides with the condensation of forsterite and enstatite, which are most of the rocky matter in solar material. Thus, microwave observations of SiS gas in other protoplanetary disks can show where rocky material condenses and Earth-like planets form.

Finally, as temperature decreases further, sulfur condenses into troilite (FeS) as H_2S gas reacts with the Fe metal grains suspended in the solar nebula

$$H_2S\ (g) + Fe\ (metal) = FeS\ (troilite) + H_2\ (g) \qquad (11)$$

Figure 2 shows that FeS begins to form at 700 K, which is the condensation temperature for troilite. The amount of FeS increases with decreasing temperature until 50% of all sulfur is in troilite and 50% is in H_2S gas at ~ 600 K, which is the 50% condensation temperature for sulfur. Figure 2 shows that the formation of troilite consumes virtually all H_2S gas by ~ 475 K. The thermochemical equilibrium calculations predict that troilite remains stable with decreasing temperature and does not react with the other nebular gases. Thus, Figure 2 shows that 100% of sulfur remains in troilite at lower temperatures.

5.3 Condensation Calculations for Elements Dissolving in Solid Solutions

Many minor and trace elements condense by dissolving in solid solutions with more abundant host phases made of major elements. For example, Au, Co, Ge, and Ni, which are less abundant than Fe, dissolve in iron metal, which is a major phase in chondrites. Likewise, the actinides (U, Th), lanthanides (or rare earth elements, REE), and lithophile transition elements (e.g., V, Nb, Ta) dissolve into the minerals hibonite $CaAl_{12}O_{19}$ and perovskite $CaTiO_3$, which occur in the Ca, Al-rich inclusions (CAIs) in the Murchison

CM and Allende CV carbonaceous chondrites. (Some major elements such as carbon and nitrogen also dissolve in solid solution in Fe metal alloy via reactions of CO (or CH_4) and N_2 (or NH_3) with metal grains. However, the amounts of carbon and nitrogen dissolved in metal are small relative to their solar elemental abundances and most C and N remain in the gas phase until they condense at low temperatures.)

The minor or trace elements begin dissolving into the host phase as soon as it condenses. The amount of an element dissolved in solid solution increases with decreasing temperature until all of an element is in the host phase. Thus, the ‘‘50% condensation temperature’’ is used to describe the condensation temperatures of minor and trace elements that dissolve in solid solution. At the 50% condensation temperature, half of an element is in the gas and the other half is in the solid condensate. For example, Ge and Ni both start to condense into Fe metal as soon as Fe metal forms, but 50% of all Ni is condensed in Fe alloy at higher temperatures than 50% of all Ge, which is more volatile. Fifty percent condensation temperatures can also be calculated for major elements, as we illustrated above for sulfur. The 50% condensation temperatures of minor and trace elements are independent of their total solar system abundance but are dependent on the availability and amount of the major host phase, which do depend on the relative abundances of the major elements.

Elemental analyses of minerals in meteorites show the important host phases for minor and trace elements. Other indicators of which mineral phases can serve as host phases are general chemical affinities of the elements and phase equilibrium studies done in materials science. In some cases, non-ideal solid solutions are used but in many cases,

the ideal solution approximation is used. The papers by Fegley and Palme [52], and Kornacki and Fegley [53] describe solid-solution condensation computations.

6 Overview of Nebular Chemistry of the Elements

Figure 4 and Table 4 give an overview of the cosmochemistry of the elements. Figure 4 shows condensation curves as a function of total pressure and the nebular P, T profile of Lewis [51] as the dashed line. For reference, the pressures given along the top of Figure 2 correspond to different temperatures along this profile. In other words, Figure 2 is a slice through Figure 4 along the dashed line. Likewise, Figure 3 is a slice through Figure 4 along the 10^{-4} bar isobar.

The condensation curves in Figure 4 show the temperatures where the different minerals become thermodynamically stable in the solar nebula gas. For example, the troilite line shows where FeS forms by reaction of H_2S gas with Fe metal. The troilite line corresponds to the point in Figure 2 where FeS starts to form. Figure 2 also shows how the abundance of FeS increases with decreasing temperature, but Figure 4 shows only where FeS starts to form.

The troilite condensation curve in Figure 4 is a horizontal line because the net thermochemical reaction for FeS formation

$$H_2S\ (g) + Fe\ (metal) = FeS\ (troilite) + H_2\ (g) \qquad (12)$$

has one gas molecule on each side of the equation. The magnetite Fe_3O_4 line in Figure 4 is also horizontal because the net thermochemical reaction for Fe_3O_4 formation

$$4H_2O\ (g) + 3Fe\ (metal) = Fe_3O_4\ (magnetite) + 4H_2(g) \qquad (13)$$

has four gas molecules on each side of the equation.

Figure 4 shows a diagonal striped band for the magnetite condensation curve because the temperature for magnetite formation depends upon the water vapor partial pressure in the solar nebula. In turn, the water vapor partial pressure depends upon the major C-bearing gases because the C/O ratio is 0.50 and formation of CO gas consumes oxygen otherwise found in water vapor. Magnetite forms at higher temperatures shown by the upper line if all carbon is present as CH_4 (as predicted by chemical equilibrium). Conversely, magnetite forms at lower temperatures shown by the lower line if all of the carbon is present as CO. Magnetite forms inside the diagonal band if part of the carbon is present as CH_4 and part is present as CO. Some or all carbon remains as CO if its reduction to CH_4 by gas phase chemistry is kinetically inhibited [23].

However, in general, condensation curves depend on the total pressure and condensation temperatures increase with increasing total pressure because gaseous reactants are consumed to make solid condensates. For example, forsterite condensation via the net thermochemical reaction

$$2Mg\ (g) + SiO\ (g) + 3H_2O\ (g) = Mg_2SiO_4\ (forsterite) + 3H_2\ (g) \qquad (14)$$

consumes five gas molecules and produces only three H_2 molecules. Rearranging the equilibrium constant (K_{eq}) expression for reaction (14) shows that the forsterite activity is proportional to total pressure squared

$$a_{Mg_2SiO_4} = \frac{X_{Mg}^2 X_{SiO} X_{H_2O}^3}{X_{H_2}^3} K_{eq} P_T^3 \qquad (15)$$

The X_i terms are the mole fractions of the different gases, K_{eq} is the equilibrium constant for reaction (14), and P_T is the total pressure. As we mentioned earlier, condensates form when their thermodynamic activity equals unity. Equation (15) shows that at constant

temperature the Mg_2SiO_4 activity increases with pressure cubed and thus forsterite reaches unit activity at a higher temperature at higher pressures.

We wrote the condensation reaction (14) for forsterite using the major gases for Mg, Si, and O that are predicted by thermochemical equilibrium calculations. Table 4 lists the major gases for all naturally occurring elements in the solar nebula. However, the net thermochemical reaction is different from the actual sequence of elementary reactions that occur during forsterite condensation. For example, one plausible mechanism is

$$SiO + OH \rightarrow SiO_2 + H \qquad \Delta H \sim -29 \text{ kJ mol}^{-1} \qquad (16)$$

$$MgO + SiO_2 \rightarrow MgSiO_3 \qquad \Delta H \sim -365 \text{ kJ mol}^{-1} \qquad (17)$$

$$MgO + MgSiO_3 \rightarrow Mg_2SiO_4 \qquad \Delta H \text{ is unknown} \qquad (18)$$

$$Mg_2SiO_4 = Mg_2SiO_4 \text{ (forsterite)} \qquad \Delta H << 0 \qquad (19)$$

The enthalpy of reaction (18) is unknown, but the other elementary reactions are exothermic and probably have small activation energies.

Figure 4 shows condensation curves for the elements (Fe, Mg, Si, S, O) that make up most of the mass of rocky planets such as the Earth. The Fe metal condensation curve is for the net thermochemical reaction

$$Fe \text{ (g)} = Fe \text{ (metal)} \qquad (20)$$

At high temperatures, all iron is monatomic Fe gas and it condenses to Fe metal at 1357 K at 10^{-4} bars total pressure (Table 4). Iron is 50% condensed by 1334 K at the same total pressure. Figure 4 and Table 4 show that the Fe metal and forsterite condensation curves intersect one another at about 10^{-4} bars total pressure. Iron condenses before forsterite at

higher pressures and after it at lower pressures. The nebular P, T profile is to the right of this intersection point because the planet Mercury is Fe-rich [51].

The condensation curve for enstatite $MgSiO_3$ is very similar to that of forsterite and is not shown in Figure 4 to simplify the graph. Enstatite condenses via the net thermochemical reaction

$$Mg_2SiO_4 \text{ (forsterite)} + SiO\ (g) + H_2O\ (g) = 2MgSiO_3 \text{ (enstatite)} + H_2\ (g) \quad (21)$$

Reaction (21) is different from forsterite condensation because it involves reaction of gases with the pre-existing forsterite grains. It is thus similar to troilite and magnetite formation, which also involve the reaction of nebular gas with pre-existing condensate grains (iron metal in these two cases).

The serpentine + brucite condensation curve represents the hydration of forsterite Mg_2SiO_4 grains by water vapor

$$2Mg_2SiO_4 \text{ (forsterite)} + 3H_2O\ (g) = Mg_3Si_2O_5(OH)_4 \text{ (serpentine)} + Mg(OH)_2 \text{ (brucite)} \quad (22)$$

An analogous reaction is formation of talc and brucite by hydration of enstatite grains

$$4MgSiO_3 \text{ (enstatite)} + 2H_2O\ (g) = Mg_3Si_4O_{10}(OH)_2 \text{ (talc)} + Mg(OH)_2 \text{ (brucite)} \quad (23)$$

These hydration reactions provide water-bearing rocky material in the inner solar nebula. By mass serpentine contains 13.0% water, talc 4.8% water, and brucite 3.1% water. But it is unclear whether chemical reaction rates are fast enough for hydration reactions to occur at the low temperatures and pressures where serpentine, talc, and other hydrous minerals are thermodynamically stable [24,54].

As mentioned above, Figure 4 shows the condensation curves for elements comprising most of the rocky material in the solar system. The elemental abundances in

Table 1 show that most of this mass is in iron metal, forsterite Mg_2SiO_4, and enstatite $MgSiO_3$. The elements Fe, Mg, and Si are called major elements, denoted by ME in Table 4. The condensation curves for enstatite, forsterite, and iron metal are also a dividing line, which separates the refractory elements at higher temperatures from the moderately volatile elements at lower temperatures. Likewise, the troilite FeS condensation curve divides the moderately volatile elements from the highly volatile elements at lower temperatures. Finally, the water ice condensation curve separates the highly volatile elements from the atmophile elements (H, C, N, O, and the noble gases), which condense at even lower temperatures. We now describe the cosmochemical behavior of the elements in each of these categories in more detail. While doing so we also explain the remaining condensation curves on Figure 3.

6.1 Refractory Elements

The refractory elements condense at temperatures above the condensation curves of iron metal and forsterite. Both lithophile (rock loving) elements and siderophile (metal loving) elements are refractory in the solar nebula.

6.1.1 Refractory Lithophiles.

The lanthanides (REE or rare earth elements), the actinides, the alkaline earths, Al, and elements in groups 3b (Sc, Y), 4b (Ti, Zr, Hf), and 5b (V, Nb, Ta) of the periodic table are included in this category. The RL in Table 4 denotes refractory lithophile elements. Table 4 lists the major gases, initial condensates, and condensation temperatures for the refractory lithophile elements. In general, the condensation chemistry of the RL elements is well known except for that of Ba, Eu, and Sr. These

elements occur in perovskite $CaTiO_3$, and the condensation temperatures in Table 4 for Ba, Eu, and Sr assume ideal solid solution in perovskite.

The refractory lithophiles occur in the Ca, Al-rich inclusions (CAIs) in Allende and other carbonaceous chondrites (CM, CV, CO, and CK chondrites, but not CI chondrites). Rarely, CAIs occur in ordinary and enstatite chondrites. The CAIs are composed of minerals rich in Ca, Al, and Ti, such as hibonite $CaAl_{12}O_{19}$; melilite, a solid solution of gehlenite $Ca_2Al_2SiO_7$ and åkermanite $Ca_2MgSi_2O_7$; spinel $MgAl_2O_4$; and perovskite $CaTiO_3$. The abundances of the refractory lithophiles in CAIs average about 20 times their solar elemental abundances because the CAIs are composed of the refractory lithophile elements that comprise 5% of the total mass of rocky material. Most of this mass is in Ca, Al, and Ti because the solar elemental abundances of the other refractory lithophiles are lower than those of Ca, Al, and Ti (see Table 1). Kornacki and Fegley [53] review the condensation chemistry of refractory lithophiles in more detail.

6.1.2 Refractory Siderophiles.

The refractory siderophiles (RS in Table 4) are the Pt-group metals (except Pd), Mo, W, and Re. Like the refractory lithophiles, they are enriched to about 20 times solar elemental abundances (on average) in CAIs. The refractory siderophiles are trace elements and their total mass is much lower than that of the refractory lithophiles. As a consequence, the refractory siderophiles occur as metal nuggets or Fremdlinge - complex multiphase assemblages of metal, oxide and sulfide - inside CAIs [55,56]. The refractory metal nuggets are condensates from the solar nebula and their compositions are reproduced by condensation calculations [52,55]. The origin of the Fremdlinge, which

means stranger in German, is more controversial and a variety of models have been proposed to explain their origin [56-59]. Each of these models has attractive features, but none explains all of the complexities observed in the Fremdlinge, and their origin is still enigmatic.

6.2 Major Elements

As mentioned above, the condensation curves for Fe metal, forsterite Mg_2SiO_4, and enstatite $MgSiO_3$ are important boundaries that separate the refractory elements at higher temperatures from the volatile elements at lower temperatures. Most of the rocky material in solar composition matter condenses out of the solar nebula gas when Fe, Mg, and Si condense. Table 4 lists the chemical behavior of these three major elements (ME).

The enstatite and forsterite that condense at high temperatures are essentially pure $MgSiO_3$ and Mg_2SiO_4 because of the low oxygen fugacity in the solar nebula gas. LeChatelier's Principle shows that the large excess of H_2 in solar composition material displaces the water vapor – hydrogen equilibrium reaction (1) toward H_2O

$$2H_2O = 2H_2 + O_2 \tag{1}$$

This leads to very small oxygen fugacities (partial pressures) given by equation (2)

$$\log fO_2 = 2\log\left(\frac{X_{H_2O}}{X_{H_2}}\right) + 5.67 - \frac{25{,}664}{T} \tag{2}$$

As noted earlier, the (H_2O/H_2) molar ratio is about 5.8×10^{-4} over a wide range of pressure and temperature conditions in the solar nebula. Equation (2) for the temperature-dependent oxygen fugacity of solar composition material then becomes

$$\log fO_2 = -0.80 - \frac{25{,}664}{T} \tag{3}$$

As a result, the amounts of ferrosilite $FeSiO_3$ in enstatite and fayalite Fe_2SiO_4 in forsterite are very small until low temperatures where reactions between Fe metal, water vapor and the pure magnesium silicates becomes thermodynamically favorable [60,61]. These net thermochemical reactions are

$$2MgSiO_3 \text{ (enstatite)} + 2Fe \text{ (metal)} + 2H_2O \text{ (gas)} = Mg_2SiO_4 \text{ (forsterite)} + Fe_2SiO_4 \text{ (fayalite)} + 2H_2 \text{ (gas)} \quad (24)$$

$$Fe_2SiO_4 \text{ (fayalite)} + 2MgSiO_3 \text{ (enstatite)} = Mg_2SiO_4 \text{ (forsterite)} + 2FeSiO_3 \text{ (ferrosilite)}$$

$$3Fe \text{ (metal)} + 4H_2O \text{ (gas)} = Fe_3O_4 \text{ (magnetite)} + 4H_2 \text{ (gas)} \quad (25)$$

At temperatures of 400 – 600 K they produce olivine and pyroxene solid solutions containing several tens of mole % of fayalite and ferrosilite. The remaining Fe metal reacts with nebular water vapor to form magnetite via reaction (26)

$$4H_2O \text{ (g)} + 3Fe \text{ (metal)} = Fe_3O_4 \text{ (magnetite)} + 4H_2\text{(g)} \quad (26)$$

Fegley [24] and Palme and Fegley [50] have questioned this picture because solid-state diffusion is very slow at the low temperatures where magnetite and Fe^{2+}-rich silicates are predicted to be thermodynamically stable. They argue that diffusion is too slow for these reactions to occur over the estimated 10^5 to 10^6 year lifetime of the solar nebula. Instead, they find that the high temperature condensation under oxidizing conditions in the solar nebular plausibly explains the observed textural features and chemistry of Fe^{2+}-rich olivines. The oxidizing conditions occur in dust-rich regions, such as the nebular midplane, where heating of the dust releases the oxygen in rock into the gas and increases the local H_2O/H_2 ratio above the typical value of 5.8×10^{-4} in a solar composition gas. Ubiquitous depletions of Mo and W in refractory metal grains in CAIs

also require oxidizing conditions at high temperatures [52]. Alternatively, photolysis of O-bearing gases such as CO and H_2O in the outer skin (photosphere) of the solar nebula may produce O_2, which would give very oxidizing conditions. Interstellar UV light and UV light from the proto-Sun may drive nebular photochemistry and produce O_2 and other disequilibrium products. In any case, many workers have discarded the notion that Fe^{2+}-rich silicates formed at low temperatures in the solar nebula. An origin by metamorphic reactions on the meteorite parent bodies is an alternative to an origin under oxidizing conditions in the solar nebula [22].

6.3 Volatile Elements

6.3.1 The Moderately Volatile Elements.

The moderately volatile (MV) elements have condensation temperatures intermediate between those of the major elements Fe, Mg, and Si and that of troilite FeS. The geochemically diverse elements in this group are Na, K, Rb, Cr, Mn, Cu, Ag, Au, Zn, B, Ga, P, As, Sb, S, Se, Te, F, and Cl. Table 4 summarizes the condensation chemistry of the moderately volatile elements, which is discussed in detail by Lodders [2]. We are mainly interested in the chemistry of phosphorus and sulfur, which are important biogenic elements (see sections 5.2 above and 6.4 below).

6.3.2 The Highly Volatile Elements.

Only a few elements fall into this category (denoted by HV in Table 4). Mercury is probably a highly volatile element but it is calculated to condense as Hg(s) at temperatures below 200 K [60]. It is unlikely that Hg is as volatile as water ice, and the low condensation temperature is probably an artifact due to incomplete thermodynamic

data on plausible condensates. The other highly volatile elements are Br, Cd, In, Tl, Pb, and Bi. The condensation chemistry of these elements is not well known. Bromine is calculated to condense as bromapatite $Ca_5(PO_4)_3Br$ at about 350 K (Fegley and Lewis [62]), but its abundance in chondrites suggests a higher condensation temperature. The elements Tl, Pb, and Bi are calculated to condense in solid solution in Fe metal while Cd and In are calculated to condense in solid solution in FeS [63]. It is difficult to model the chemistry of these elements because of incomplete and uncertain thermodynamic data for solid solution of these elements and their compounds in host phases such as FeS and Fe metal. The meteoritic host phases of several highly volatile elements are also unclear.

6.4 Phosphorus.

Phosphorus is the sixth most abundant element in the human body (6300 μg/g), the eleventh most abundant element in phytomass (52 μg/g), and the twelfth most abundant element in Earth's crust (757 μg/g). Phosphorus in the crust occurs in orthophosphate minerals and phosphorite rock, which has about the same composition as fluorapatite $Ca_5(PO_4)_3F$. Phosphorus is an essential nutrient and an important fertilizer. A solid solution of hydroxyapatite and fluorapatite $Ca_5(PO_4)_3(OH,F)$ is a key constituent of tooth enamel, calcium phosphates are key constituents of bones, and organophosphates are part of the nucleic acids DNA and RNA, and the molecules ADP (adenosine diphosphate $C_{10}H_{15}O_{10}N_5P_2$) and ATP (adenosine triphosphate $C_{10}H_{16}O_{13}N_5P_3$), which supply energy in metabolic processes.

Figure 5, based on the results of Fegley and Lewis [62], summarizes phosphorus chemistry in the solar nebula. Figure 5, like Figure 2 for sulfur, is along the nebular P, T

profile in Figure 4. It shows the percentage distribution of phosphorus between gases and solids that are thermodynamically stable in solar composition material. Phosphorus gas phase chemistry is complex with seven gases comprising 1% or more of the total phosphorus abundance. Monatomic P gas is the major gas at high temperatures but it is converted into molecular gases, mainly PN, PO, PH, PH_2, PS and P_2 with decreasing temperature. Two of these gases, PN and PO, are observed interstellar molecules. Phosphorus condenses as schreibersite Fe_3P at ~ 1225 K by reaction of P-bearing gases with preexisting Fe metal grains. Schreibersite is a common trace mineral in iron, stony iron, and stony meteorites. Small amounts of phosphorus also dissolve in Fe metal alloy, but most phosphorus goes into schreibersite. As shown in Table 1, the solar elemental abundance of Fe is about 100 times larger than that of phosphorus. Thus, condensation of Fe_3P removes all phosphorus from the gas and consumes only a small percentage of Fe metal. Water vapor oxidizes about 35% of the Fe_3P to fluorapatite $Ca_5(PO_4)_3F$ at 766 K. Fluorine is less abundant than P and limits the amount of fluorapatite formed. The remaining Fe_3P is oxidized by water vapor to whitlockite $Ca_3(PO_4)_2$ at 714 K. Whitlockite is destroyed by reaction with water vapor at ~ 460 K to form hydroxyapatite $Ca_5(PO_4)_3OH$. This is the first condensate that contains water (two hydroxyapatite molecules give one water molecule, ~ 1.8% H_2O by mass). Bromine reacts with some of the apatite minerals to form bromapatite $Ca_5(PO_4)_3Br$ at about 350 K, but this does not appear on Figure 5 because the Br abundance is so small (<0.14% of the P abundance).

6.5 Water

Water vapor is either the first or the second most abundant oxygen-bearing gas in solar composition material. At high temperatures and low pressures, CO is the thermodynamically stable form of carbon and the major carbon-bearing gas. Table 1 shows that the solar C/O atomic ratio is 0.50 and thus 50% of total oxygen is in CO gas. The remaining 50% of total oxygen is in H_2O, SiO, OH, AlOH, Al_2O, PO, other metal oxide gases, and oxide and silicate minerals that condense from the solar nebula. As a result, CO is slightly more abundant than H_2O and is the major O-bearing gas at high temperatures and low pressures. The CO/H_2O equal abundance curve is given in Figure 3 of [19]. The thermal dissociation of water vapor to H atoms and OH hydroxyl radicals becomes more important at high temperatures, but the H_2O/OH equal abundance line is at very high temperatures (> 5000 K, Figure 3 of [19]) that would be inside the photosphere of the proto-Sun.

Assuming complete chemical equilibrium, reaction (4) converts CO into CH_4 with decreasing temperature and water vapor becomes the major O-bearing gas, e.g., see Figure 3 of [19]. However, not all oxygen is in water vapor because some of it is in the oxide and silicate minerals that condense from the solar nebula. The solar abundances in Table 1 dictate that condensation of anhydrous minerals consumes about 23% of all oxygen atoms leaving about 87% of total oxygen in H_2O.

The formation of hydrated minerals such as serpentine $Mg_3Si_2O_5(OH)_4$, brucite $Mg(OH)_2$, and talc $Mg_3Si_4O_{10}(OH)_2$ removes some more H_2O from the gas. However, as shown in Figure 4, the hydration reactions occur at low temperatures. Theoretical models of gas – grain kinetics predict that hydration of forsterite and enstatite to serpentine and

talc are too slow to proceed over the lifetime of the solar nebula [24]. These predictions are consistent with petrological studies of meteorites containing hydrous silicates, which conclude that hydrous minerals formed on the meteorite parent bodies. The implication is that water ice condensed on the meteorite parent bodies and reacted with anhydrous minerals during thermal metamorphism.

Figure 4 shows the condensation curve for water ice. The water ice condensation temperature as a function of total pressure (P_T) in solar composition material is

$$\frac{10{,}000}{T_C(H_2O)} = 38.84 - 3.83 \log_{10} P_T \qquad (27)$$

Thus, water ice starts to condense at 185 K at 10^{-4} bars total pressure in solar composition material. Fifty percent of all water condenses by 180 K. Liquid water condenses instead of water ice at total pressures of ~ 3.8 bars and above. Condensation of liquid water has important consequences such as the formation of aqueous NH_3 solutions. Aqueous NH_3 solutions are stable down to 173 K at one bar total pressure, which is the eutectic point, i.e., the lowest melting point [64]. The condensation curve for water is an important boundary that separates the condensation of rocky material in the inner solar nebula from the condensation of icy material in the outer solar nebula.

6.6 Low Temperature Ices

The low temperature chemistry of solar composition material involves formation of pure ices and/or clathrate hydrates, which are compounds formed by gases trapped inside the water ice crystal structure. Clathrate hydrates are important for CH_4 and other light hydrocarbons and form inside natural gas pipelines unless the gas remains dry. The condensation temperatures for clathrate hydrates and ices increase with increasing total

pressure. For example, the condensation temperature of water ice increases by about 10 – 20 Kelvin for a tenfold increase in total pressure. We give condensation temperatures at 10^{-4} bar total pressure in our discussion below.

Water ice is the first low temperature ice that condenses (see above). Assuming complete chemical equilibrium all carbon is present as CH_4 and all nitrogen is present as NH_3 at low temperatures. Both of these combine with water ice to form other low temperature ices. Ammonia condenses as ammonia monohydrate $NH_3 \cdot H_2O$ at 131 K, 10^{-4} bars total pressure via the net reaction

$$NH_3\ (g) + H_2O\ (ice) = NH_3 \cdot H_2O\ (ice) \qquad (28)$$

Ammonia monohydrate (also called ammonium hydroxide NH_4OH) is a distinct compound and is not a clathrate hydrate. It forms at a higher temperature than either pure NH_3 ice or liquid NH_3, which do not form in the solar nebula. Ammonia ice and/or liquid NH_3 could form in the absence of water. This happens in Jupiter's atmosphere where NH_3 ice clouds form because gravitational sedimentation keeps liquid water droplets in a cloud layer hundreds of kilometers below the NH_3 ice clouds. Thus, no water is present in the upper atmosphere where the NH_3 ice clouds form. Liquid NH_3 does not condense in the solar nebula or on Jupiter or the other gas giant planets in our solar system because the total pressure and/or NH_3 gas abundance is too low. The NH_3 gas pressure would have to be at least as high as the triple point pressure (0.06 bars at 195.5 K) for liquid NH_3 condensation. The mole fraction of total nitrogen in solar composition gas at low temperatures (where there is no atomic H) is

$$X_{\Sigma_N} = \frac{A(N)}{A(H_2 + He)} = \frac{1.95 \times 10^6}{\left(1.2155 \times 10^{10} + 2.343 \times 10^9\right)} = 1.35 \times 10^{-4} \qquad (29)$$

Assuming that all nitrogen is present as NH_3, the total nebular pressure or atmospheric pressure at low temperatures would have to be about 444 bars for liquid NH_3 to form (i.e., to reach 0.06 bars NH_3 pressure at the triple point). Such high pressures are unreasonable for the solar nebula but they may occur in extrasolar gas giant planets or in the interiors of icy planets and satellites.

Table 1 shows that nitrogen is much less abundant than oxygen in solar composition material (the N/O atomic ratio is 0.14). Thus, condensation of $NH_3 \cdot H_2O$ removes all NH_3 from the solar nebula gas and excess water ice remains. This ice reacts with CH_4 and forms methane clathrate hydrate via the net reaction

$$CH_4\ (g) + 7H_2O\ (ice) = CH_4 \cdot 7H_2O\ (clathrate\ hydrate) \qquad (30)$$

Methane clathrate hydrate forms at 78 K, 10^{-4} bars total pressure and condenses at a higher temperature than pure CH_4, which forms at 41 K, 10^{-4} bars. The CH_4 clathrate hydrate and pure CH_4 ice both condense because $CH_4 \cdot 7H_2O$ formation consumes all the remaining water ice and leaves excess CH_4 gas. This situation is a natural consequence of the solar elemental abundances of carbon and oxygen (C/O = 0.50) and the 7:1 ratio of H_2O to CH_4 in the clathrate hydrate.

The chemistry of the noble gases He, Ne, Ar, Kr, and Xe in solar composition material is simple. All are present in the gas as the monatomic elements and Ar, Kr, and Xe condense as pure ices or as clathrate hydrates (if sufficient water ice is present or if they form solid solutions with CH_4 clathrate hydrate). Table 4 gives condensation temperatures for Ar, Kr, and Xe clathrate hydrates, but the pure ices form at lower

temperatures. Table 4 lists condensation temperatures for solid He and Ne, but it is unlikely that temperatures in the solar nebula were low enough for either gas to condense.

7. Cosmochemistry of Carbon and Nitrogen

We briefly described carbon and nitrogen chemistry in section 2 where we noted that the H_2 excess in solar composition material leads to formation of CH_4, NH_3, and other hydrides, especially with decreasing temperatures. Figures 6-10 provide more information about the equilibrium chemistry of carbon and nitrogen as a function of temperature and pressure in solar composition material.

7.1 Carbon Cosmochemistry

In general, the equilibium chemistry of carbon in solar composition material is fairly simple over pressures and temperatures thought to prevail in the solar nebula and other protoplanetary disks. Figure 6 shows that CO and CH_4 are the two major C-bearing gases over wide P, T ranges in solar composition material. The solid line labeled CO/CH_4 is the line in P – T space along which the two gases have equal abundances. Carbon monoxide is the major C-bearing gas at high temperatures and low pressures (above the line) while CH_4 is the major C-bearing gas at low temperatures and high pressures (below the line). As noted earlier, the net thermochemical reaction converting the two gases is

$$CO + 3H_2 = CH_4 + H_2O \quad (4)$$

$$\log K_1 = 11{,}069.94/T - 1.17969 \log T - 8.96596 \quad (5)$$

Equation (5) gives the equilibrium constant for reaction (4) from 298 – 2500 K.

However, it is important to realize that CO and CH_4 are present on both sides of the dividing line and do not disappear once the other gas becomes the major C-bearing

gas. This is a common misconception because the CO/CH_4 equal abundance line is not strictly analogous to a phase boundary. Figures 7 and 8, which show the distribution of carbon between different C-bearing gases as a function of temperature along the 10^{-4} bar isobar, emphasize this point. Figure 7 displays the percentage distribution of carbon between its three most abundant gases CO, CH_4, and CO_2 and Figure 8 shows the mole fractions of a larger number of carbon gases.

Figure 7 shows the gradual decrease in CO and simultaneous increase in CH_4 with decreasing temperature along the 10^{-4} bar isobar (i.e., Figure 7 is a slice through Figure 6 along this isobar). The isobar crosses the equal abundance line in Figure 6 at 625 K where CO and CH_4 have abundances of ~ 50% each. Their abundances are slightly less than 50% because the abundance of CO_2 increases to ~ 0.5% of total carbon at this point. Carbon monoxide is easily converted to CO_2 via the rapid elementary reaction

$$\mathrm{CO + OH \rightarrow CO_2 + H} \tag{31}$$

Baulch et al [65] give the recommended rate constant for this reaction from 250 – 2500 K (with ± 50% uncertainty) as

$$\log_{10} k = 3.94\times10^{-4} T - 12.95 \ \mathrm{cm^3\ molecule^{-1}\ s^{-1}} \tag{32}$$

The reverse elementary reaction converting CO_2 into CO is also rapid

$$\mathrm{CO_2 + H \rightarrow CO + OH} \tag{33}$$

The recommended rate constant from 1000 – 3000 K (with ± 20% uncertainty) from Baulch et al [65] is

$$k = 2.50\times10^{-10} \exp(-13{,}300/T) \ \mathrm{cm^3\ molecule^{-1}\ s^{-1}} \tag{34}$$

Consequently, CO and CO_2 remain in chemical equilibrium down to low temperatures and CO_2 comprises a small fraction (about 0.5 – 1%) of total carbon in the solar nebula. As discussed by Lewis and Prinn [23], the CO_2 eventually condenses as solid CO_2 (dry ice), ammonium bicarbonate NH_4HCO_3, or ammonium carbamate (NH_4COONH_2). Carbon dioxide is the major C-bearing gas at low temperatures and pressures below 408 K, 10^{-9} bars [19,66]. Figure 2 and the associated discussion in Lodders and Fegley [19] describe the complex equilibrium chemistry of carbon at these low temperatures and pressures.

The intersection of the CO and CH_4 curves in Figure 8 marks the CO/CH_4 equal abundance point at 10^{-4} bars total pressure. The peak in the CO_2 curve at this point occurs because the graphite activity reaches a maximum along the CO/CH_4 equal abundance line [66]. The peaks in the COS, HCN, and C_2H_6 curves do not correspond exactly with this peak activity because their abundances are influenced by other factors as well (e.g., sulfur condensation as FeS, N_2 conversion to NH_3, and the dominance of H_2).

The thermodynamic activity of graphite peaks along the CO/CH_4 equal abundance line and reaches a maximum value of ~ 0.1 near the intersection of the nebular P, T profile with the CO/CH_4 equal abundance line (e.g., see Figure 1 of [66]). The relatively high graphite activities mean that significant amounts of carbon can dissolve in Fe metal grains in the solar nebula.

Lewis et al. [66] calculated a maximum dissolved carbon concentration in Fe-Ni metal of 50 μg/g, at 750 K along the nebular P, T profile (see their Figure 3). This is equivalent to ~ 15 μg/g carbon in chondritic material and is less than the typical carbon

concentrations of 1200 – 2350 μg/g in ordinary chondrites (Table 1 of [67]). Lewis et al. [66] concluded that the equilibrium carbon concentrations predicted in chondritic material were several times smaller than actually observed.

Apparently, most of the carbon in ordinary chondrites is in organic material formed by disequilibrium processes such as Fischer-Tropsch type reactions (Anders et al. [68]) or Miller-Urey reactions [69]. The hydrogen contents in ordinary chondrites range from 360 – 670 μg/g based on the mean H_2O^+ contents for H, L, LL chondrites in Table 1 of Schaefer and Fegley [67]. These hydrogen contents suggest the presence of organic material because very few hydrous minerals are observed in these meteorites. However, some hydrous minerals are found in the unequilibrated ordinary chondrites (UOCs, metamorphic grades 3.0 – 3.9) that are less thermally metamorphosed than the equilibrated ordinary chondrites (metamorphic grades 4 – 7).

As noted above the maximum graphite activity reaches ~ 0.1 in the solar nebula. However, formation of pure graphite requires only occurs when its thermodynamic activity reaches unity. The maximum temperature and pressure for graphite stability in solar composition material are 463 K, 4.32×10^{-8} bars (see Figure 2 in [19]). However, the region of most interest for us is closer to the intersection of the nebular P, T profile with the CO/CH_4 equal abundance line. This occurs at about 625 K, 10^{-4} bars and is a likely region for grain-catalyzed conversion of CO to organic compounds via Fischer-Tropsch type (FTT) reactions.

7.2 Nitrogen Cosmochemistry

The equilibrium chemistry of nitrogen in solar composition material is simple. The two major N-bearing gases are N_2 and NH_3 (see Figures 6 and 9). They are converted into one another by the net thermochemical reaction

$$N_2 + 3H_2 = 2NH_3 \tag{35}$$

$$\log K = 6051.59/T - 1.21176 \log T - 7.89739 \tag{36}$$

Equation (36) gives the equilibrium constant from 298 – 2500 K for reaction (35). Chemical equilibrium calculations using this data and the solar elemental abundances show that N_2 is the dominant N-bearing gas at high temperatures and low pressures and that NH_3 is the major N-bearing gas at low temperatures and high pressures. Figures 6 and 9 summarize these results. Figure 6 shows the N_2/NH_3 equal abundance line over a wide P, T range, while Figure 9 shows the percentage distribution of nitrogen between N_2 and NH_3 from 300 – 700 K. At higher temperatures, N_2 is the only nitrogen-bearing gas of any importance. Along the 10^{-4} bar isobar, NH_3 remains the second most abundant N-bearing gas until about 1670 K where monatomic N becomes the second most abundant gas. However, even at 2000 K, 10^{-4} bars the N_2/N molecular ratio is 100,000 and all other N-bearing gases are less abundant, as shown in Figure 10.

The N_2/NH_3 equal abundance line is slightly different from the CO/CH_4 equal abundance line because equal abundances of N_2 and NH_3 do not correspond to 50% of total nitrogen in each gas. A comparison of Figures 6 and 9 shows that at 10^{-4} bars total pressure, N_2 and NH_3 have equal abundances at 345 K but 50% of total nitrogen is in each gas at 320 K. At lower temperatures, NH_3 first condenses as ammonium carbonate NH_4HCO_3, or ammonium carbamate (NH_4COONH_2). The exact amount of NH_3 in these

compounds depends upon the amount of CO_2 and is hard to quantify because the amount of CO_2 depends on the rate of nebular mixing and of the CO to CO_2 conversion. The remaining NH_3 condenses as ammonia monohydrate ($NH_3 \cdot H_2O$) at 131 K, 10^{-4} bars.

However, the gas phase conversion of N_2 to NH_3 is a slow reaction and may not occur over the lifetime of the solar nebula [23]. Industrial production of NH_3 from N_2 (the Bosch – Haber process) uses Fe-based catalysts to speed up the reaction. Iron-rich metal grains and magnetite Fe_3O_4 grains are common in chondritic meteorites and it is likely that such grains catalyzed the N_2 to NH_3 conversion in the solar nebula [23].

8. Grain Catalyzed Conversion of CO to Organic Compounds

As mentioned above, Fe metal alloy grains in the solar nebula may catalyze a number of reactions including CO reduction to CH_4, N_2 reduction to NH_3, and the synthesis of organic molecules from the CO + H_2 in nebular gas via Fischer-Tropsch type reactions. The latter possibility was anticipated by Urey [70] who proposed that the CO to CH_4 conversion in the solar nebula "may well proceed through graphite or complex tarry compounds as intermediates. Such compounds have long been known to be constituents of the carbonaceous chondritic meteorites."

At chemical equilibrium CO converts to CH_4 with decreasing temperature and/or increasing pressure, but theoretical models of the reaction mechanism predict CO reduction proceeds slowly if at all, e.g. [23]. This should not be surprising because the gas phase reduction of CO to CH_4 is a reverse combustion reaction that converts CO, a product of incomplete combustion, back to CH_4, which is an easily combustible fuel. Their prediction can be tested by experimental studies of the elementary reactions

involved in the gas phase reduction of CO to CH_4 in H_2-rich and C-poor gases. High spatial resolution infrared spectra of CO and CH_4 in the inner regions of protoplanetary disks can also test this prediction. Neither data set is available at present.

Heterogeneous catalysis of CO reduction to CH_4 in the solar nebula and other protoplanetary accretion disks is important for a number of reasons including the types of carbon-bearing ices in icy bodies, the water ice/rock ratio of icy bodies, the nebular oxidation state, the carbon content of metal equilibrated with nebular gas, and organic compound formation. The heterogeneous catalysis of N_2 reduction to NH_3 is important for a number of reasons including the types of nitrogen-bearing ices in icy bodies, the melting point depression caused by dissolved NH_3, the presence of electrically conductive fluid regions giving rise to magnetic fields on icy bodies, the generation of cryovolcanic fluids, and organic compound formation. Grain-catalyzed chemistry may also produce the saturated compounds in circumstellar outflows from cool carbon stars [71].

A large industrial literature on synthetic fuel production shows that CO is reduced to CH_4, alkanes, alkenes, and alcohols by Fischer-Tropsch type (FTT) reactions that are catalyzed by Fe and other transition metals [72]. Industrial FTT reactions use a Fe or Co based catalyst to convert a CO/H_2 gas mixture into hydrocarbons such as gasoline. Alkanes such as methane CH_4, ethane C_2H_6, propane C_3H_8, n-butane C_4H_{10}, and so on form via net FTT reactions such as

$$nCO + (2n + 1)H_2 = C_nH_{2n+2} + nH_2O \quad (37)$$

$$2nCO + (n+1)H_2 = C_nH_{2n+2} + nCO_2 \quad (38)$$

Alkenes such as ethylene C_2H_4, propylene C_3H_6, butylene C_4H_8, and so on form via net FTT reactions exemplified by

$$nCO + 2nH_2 = C_nH_{2n} + nH_2O \quad (39)$$

$$2nCO + nH_2 = C_nH_{2n} + nCO_2 \quad (40)$$

Methanol (CH_3OH) and other alcohols form via net FTT reactions such as

$$nCO + 2nH_2 = C_nH_{2n+1}OH + (n - 1)H_2O \quad (41)$$

$$(2n - 1)CO + (n + 1)H_2 = C_nH_{2n+1}OH + (n - 1)CO_2 \quad (42)$$

The distribution of products between alkanes, alkenes, and alcohols, and within each class of compounds, depends upon the reaction conditions and catalysts.

The industrial literature, e.g. [73,74], experiments by our group [75], and by many other scientists also show that carbonaceous material similar to asphalt or tar forms on and eventually deactivates the catalyst during FTT reactions. The formation of iron carbides ranging in composition from Fe_2C to Fe_3C on the catalyst is also common. These results are interesting because the carbonaceous coatings and iron carbides that form on the catalysts may be similar to the “tar balls” and iron carbides observed in interplanetary dust particles [76,77] and to the polymeric organic material in carbonaceous chondrites [78,79]).

In the 1960s and 1970s Anders and colleagues studied Fischer-Tropsch type (FTT) reactions using Fe based catalysts and mixtures of CO, H_2, and NH_3 [68,80]. They produced a variety of organic compounds and argued that organic compounds in meteorites were produced by FTT reactions in the solar nebula. However, their experiments were done at atmospheric pressure with CO/H_2 ratios much larger than the

CO/H_2 ratio of 582 parts per million by volume (ppmv) for solar composition gas with all carbon present as carbon monoxide.

More recently, Llorca and Casanova [81] studied formation of carbonaceous material in interplanetary dust particles (IDPs). Interplanetary dust particles are micrometer sized particles of chondritic material that are not destroyed upon entry into Earth's atmosphere. The IDPs are collected on oil-coated surfaces inside the wings of specially modified U2 aircraft flying in the stratosphere. Llorca and Casanova [81] heated a $CO-H_2$ gas mixture containing 4,000 ppmv CO with a silica supported Fe-Ni catalyst in a sealed vessel for 1,000 hours. They did experiments at 473 K and 5×10^{-4} bar total pressure and found that carbonaceous material and a metal carbide $(Fe,Ni)_2C$ formed on the catalyst and that hydrocarbons formed in the gas phase. Under their experimental conditions, Llorca and Casanova [81] found that Fe-Ni alloy catalyzes conversion of CO to CH_4 with only smaller amounts of $C_2 - C_4$ alkanes and alkenes. The hydrocarbons were dominantly CH_4 (90%), with smaller amounts of C_2H_6 (~5%), C_2H_4 (~2%), C_3H_8 (~2%), C_3H_6 (0.5%), and C_4H_{10} (0.4%).

Fegley and Hong [75] obtained similar results to those of Llorca and Casanova [81]. They experimentally studied heterogeneous catalysis of reactions between CO and H_2 in H_2-CO gas mixtures containing 740 parts per million by volume (ppmv) CO. The experiments were done at atmospheric pressure in a flow system with different catalysts placed in an alumina boat in the isothermal hot zone of a furnace. The reacted gas was analyzed by gas chromatography and standard gas mixes were used for identification and quantification of the products. The catalyst surface area before and after reaction was

measured by the N_2 gas absorption (BET) method. The empty alumina boat, high purity iron metal, the Gibeon iron meteorite, the Gao H5 ordinary chondrite, terrestrial olivine ($Fa_{10}Fo_{90}$, green sand from Hawaii), a commercial NH_3 synthesis catalyst (KMR1), terrestrial magnetite, and platinum gauze were used as catalysts. Fegley and Hong [75] produced only methane and water vapor under their experimental conditions. They measured the amount of CH_4 produced as a function of temperature and per mm^2 of catalyst at constant gas flow rates to obtain data on the efficiency of different catalysts. Figure 11 compares CH_4 yields from several different catalysts as a function of temperature and shows that the most CH_4 is produced using an iron metal catalyst. The Gao H5 chondrite and terrestrial olivine (green sand from Hawaii with 10-mole % fayalite Fe_2SiO_4) also show significant catalytic activity. The latter observation is important because olivine is a major mineral in ordinary chondrites and contains 10-30 mole % fayalite. However, very little CH_4 forms when no catalyst is used and gas is passed over the empty alumina boat used to hold the catalysts. Figure 12 compares CH_4 yields at 800 K for different catalysts per mm^2 surface area. This comparison includes platinum metal and the Gibeon iron meteorite. Once again, iron metal is the best catalyst and gives the most methane per unit area. The Gao H5 ordinary chondrite is the worst catalyst and gives the least methane per unit area. Gao, and other ordinary chondrites, contain FeS, and sulfur is a catalyst poison. The presence of sulfur and/or the coating of Fe metal grains by FeS is often invoked as an argument against Fe metal catalyzed chemistry in the solar nebula. However, although Gao is less active than other catalysts, it still catalyzes CO reduction to CH_4.

Fegley and Hong [75] also measured the CH_4/H_2O ratios in the product gas and showed that the net reaction being catalyzed is

$$CO + 3H_2 = CH_4 + H_2O \quad (4)$$

because the measured CH_4/H_2O ratios are unity within error. Thus, essentially all CO is reduced to methane without significant production of higher hydrocarbons. If hydrocarbon production were significant, the measured CH_4/H_2O ratios would be less than unity and the measured hydrocarbon to water ratios would be 2 for C_2 alkane dominated products, 3 for C_3 alkane dominated products, and so on. This can be seen from the net thermochemical reaction

$$nCO + (2n + 1)H_2 = C_nH_{2n+2} + nH_2O \quad (37)$$

Fegley and Hong [75] also studied the effects of catalyst aging because sometimes a catalyst loses its activity over time. Figures 13 and 14 show data from two experiments with a commercial NH_3 synthesis catalyst (KM1R) and terrestrial magnetite separated from the Hawaiian green sand. The two catalyst samples were heated at the same temperature in the H_2-CO gas mixture for 28 days. A gas chromatograph with an automated gas-sampling valve monitored CH_4 production as a function of time. Each data point is the average of several analyses made at the same time and the error bars are one-sigma errors. The data in the figures are not normalized to the different surface areas of the two catalyst samples, so they do not give data on the different efficiencies of the two catalysts. The commercial NH_3 synthesis catalyst KM1R (Figure 13) maintained the same activity (with some fluctuations) over time while the terrestrial magnetite (Figure 14) was initially more active, then maintained a constant, but lower activity for the rest of the run.

Further work is needed to do longer time experiments and to characterize the involatile organic products formed on the catalysts.

However, the simulation experiments provide guidelines for estimating the amount of CO converted into organic compounds by Fischer-Tropsch type reactions in the solar nebula. Fegley [24] modeled the rate of nebular FTT reactions by assuming that reactions require collision of CO molecules with Fe alloy grains. Hydrogen molecules are absorbed on the Fe alloy grains already. Some of the collisions, that have the necessary activation energy, lead to formation of CH_4 and other molecules. The remainder of the collisions, that do not have the necessary activation energy, are non-reactive. The total collision rate S_i (molecules cm^{-2} s^{-1}) of CO molecules with Fe alloy grains is

$$S_i = 2.635 \times 10^{25} \left[\frac{P_{CO}}{(\mu_{CO} T)^{1/2}} \right] \tag{43}$$

The partial pressure and molecular weight of CO are P_{CO} and μ_{CO}, and T is the absolute (Kelvin) temperature. The total number of collisions N_i of CO molecules with all Fe grains per cm^3 of the solar nebula is

$$N_i = S_i A_{grain} \tag{44}$$

The A_{grain} is the total surface area of all Fe alloy grains per cm^3 of the solar nebula. This was calculated assuming that all Fe alloy grains were monodisperse, spherical, fully dense, and uniformly distributed in the nebular gas. The Fe alloy grains in chondrites are about 200 μm in diameter, while interplanetary dust particles (IDPs) contain much smaller grains 0.2 μm in diameter. The fraction of reactive collisions F_i is

$$F_i = N_i \exp\left(-\frac{E_a}{RT}\right) \tag{45}$$

The terms in the exponential are the activation energy E_a, the ideal gas constant R, and the Kelvin temperature. An activation energy of 90 kJ mol^{-1} is appropriate according to the work of Hayatsu and Anders [80] and Dry [72]. Using these values, solar abundances for CO and Fe, and assuming 200 μm diameter Fe grains, Fegley [24] found that 10% of all CO can undergo FTT reactions at 510 K over the nebular lifetime of 10^{13} seconds (about 320,000 years). This lifetime is within the 1 – 2 million-year duration for terminal accumulation of the Sun in Cameron's solar nebula model [25]. If smaller Fe grains, like those in IDPs predominate, 10% of all CO can react within 10^{13} seconds at 440 K. These calculations show that 10% of the CO gas can be converted into organic material by FTT reactions within the lifetime of the solar nebula.

9. Carbon and Nitrogen in Meteorites

Tables 5 and 6 summarize data on the carbon and nitrogen contents of chondritic meteorites. We are interested in these data because cosmochemists and geochemists believe that the Earth and other terrestrial planets accreted from a mixture of chondritic materials in the solar nebula [67]. Thermal outgassing reactions released the volatile elements in chondritic material during and/or after accretion of the Earth, Venus, and Mars and produced the early atmospheres on these planets.

The tables list the absolute concentrations of carbon and nitrogen in milligrams per gram (mg/g) for the major classes of carbonaceous (CI, CM, CV), ordinary (H, L, LL), and enstatite (EH, EL) chondrites. The data in Tables 5 and 6 are mean values computed from data in the METBASE database [82]. Comparison of the C/Si and N/Si

ratios in chondrites to those in solar composition material shows the fraction of total C and N retained in the chondritic meteorites. This fraction corresponds to about 10.9% and 2.9% of the solar carbon and nitrogen abundances, respectively, in the volatile-rich CI chondrites. (Interestingly, ureilites, a class of achondritic meteorites, contain up to 7% carbon, more than in CI chondrites. This occurs mainly as intergrowths of graphite and diamonds. The diamonds formed from the graphite by impacts. Small amounts of organic material are also present.) The other types of chondrites contain less carbon and nitrogen, but all chondrites are more volatile-rich than the Earth, which has only about 0.003% of the solar carbon and 0.002% of the solar nitrogen abundances [43]. Thus, accretion of only small amounts of volatile-rich chondritic material gives the terrestrial inventory of carbon and nitrogen.

Carbon occurs as carbon dissolved in Fe alloy, carbides, carbonates, diamond, graphite, organic matter, and poorly graphitized carbon in chondrites. In general, the carbon inventories for different chondrites and different types of chondrites are poorly known, if at all. Nitrogen occurs as N dissolved in Fe alloy, N dissolved in silicates, nitrides, organic matter, and possibly as ammonium salts (in CI chondrites). The nitrogen inventories are also poorly known, if at all.

9.1 Enstatite Chondrites

Most of the carbon in the enstatite chondrites is graphite, C dissolved in Fe alloy, or cohenite $(Fe,Ni)_3C$, also known as cementite in the metallurgical literature. The EH3-4 chondrites, which are less metamorphosed than other enstatite chondrites, also contain presolar SiC and diamonds [42]. As mentioned earlier in section 4, graphite and SiC are

stable condensates under the highly reducing conditions required for formation of the enstatite chondrites [20,21]. However, only presolar SiC grains occur in the enstatite chondrites. Hayes [79] reviews conflicting results about the presence of organic matter in the enstatite chondrites. About 1 μg/g of n-alkanes was extracted from the Indarch EH4 chondrite but no soluble organics were found in the Pillistfer EL6 chondrite. These reports are consistent with the presence of organic material in lower metamorphic grade meteorites, but are inconclusive. More work is needed to determine whether or not significant amounts of organic matter occur in the enstatite chondrites, and if any correlations exist with metamorphic grade.

Most of the nitrogen in enstatite chondrites is in nitride minerals and dissolved in silicate minerals [83]. The major nitride minerals are sinoite Si_2N_2O, osbornite TiN, and nierite α-Si_3N_4. Isotopic analyses of Si and N indicate that most of the nierite grains formed in the solar system and are not presolar [84,85]. However, it is unclear if nierite condenses in highly reduced regions of the solar nebula or forms during metamorphism on the meteorite parent body. Bischoff et al. [86] studied 31 enstatite chondrites and found that sinoite occurs only in metamorphosed EL chondrites. Osbornite is a nebular condensate at the high C/O ratios needed to form enstatite chondrites [22]. Presumably, osbornite is the source of nitrogen for making sinoite (and possibly nierite) during metamorphism. Nitrogen dissolution into silicates plausibly occurs during metamorphism because the N_2 partial pressure is higher during metamorphism on meteorite parent bodies than in the solar nebula because the outgassed volatiles contain much less hydrogen than solar composition gas in the nebula.

9.2 Ordinary Chondrites

The H (high iron), L (low iron), LL (low total iron, low iron metal) chondrites comprise the ordinary chondrites, which are the most abundant class of meteorites. Most of the carbon in ordinary chondrites is present as C dissolved in Fe metal, poorly graphitized carbon, cohenite $(Fe,Ni)_3C$, and organic matter. Carbon also occurs in presolar diamonds (36 – 130 μg/g) and SiC (0.008 – 1.5 μg/g) in unequilibrated ordinary chondrites [42]. We use mass balance calculations to estimate the carbon budget in ordinary chondrites.

A high-resolution mass spectrometric study of the Holbrook L6 chondrite by Hayes and Biemann [87] showed 50 μg/g of an aromatic organic polymer. Holbrook contains 60 μg/g carbon [87]. The aromatic organic polymer in the Orgueil CI chondrite is about 70% C by mass [79]. Assuming a similar composition for the organics in Holbrook, about 60% (36 μg/g) of all carbon is in the organic polymer. Holbrook contains about 7.2% Fe metal [82]. Assuming this contains 100 μg/g carbon, which is the average value for metal in iron meteorites [66], about 7 μg/g carbon is present as C dissolved in metal. Trace amounts of cohenite Fe_3C (250 μg/g, 0.025%) and/or poorly graphitized carbon probably account for the remaining 17 μg/g carbon.

The nitrogen inventories of ordinary chondrites are even less well known and we use mass balance calculations to give a nitrogen budget. The average nitrogen contents of ordinary chondrites are 34 – 50 μg/g (Table 6). Some of the nitrogen is dissolved N in γ-Fe,Ni (taenite) alloy (~ 10 μg/g dissolved N on average), although non-magnetic nitrogen-bearing phases are also present [88]. The average metal contents of LL, L, and H chondrites are 2.64, 7.27, and 16.72 % by mass, respectively [67]. The average

dissolved N content of 10 μg/g thus corresponds to only ~ 0.3, 0.7, and 1.7 μg/g, respectively, which is a small fraction of total nitrogen in ordinary chondrites. The aromatic polymer in Orgueil contains 1.6% N by mass [79]. Assuming 50 μg/g organic polymer, as found in Holbrook, containing 1.6% N, about 0.8 μg/g organic N is present in ordinary chondrites. Russell et al. [85] report 0.012 – 0.148 μg/g nierite in the ordinary chondrites they studied. Nierite is 40% N by mass, and thus accounts for only a tiny amount of the total nitrogen budget. These mass balance calculations show that most of the nitrogen in ordinary chondrites is not in metal, nierite, or organics and must be elsewhere, probably dissolved in silicate minerals or in other trace nitride minerals. A small amount of nitrogen may also be dissolved in carbides and in presolar diamonds in the unequilibrated ordinary chondrites

9.3 Carbonaceous Chondrites

We focus on the CI and CM carbonaceous chondrites because the CV and other carbonaceous chondrites are relatively poor in carbon and nitrogen. The carbon in CI and CM chondrites is mainly in organic material with the rest in carbonates, whewellite $Ca(C_2O_4)\cdot H_2O$ (calcium oxalate monohydrate), and presolar grains. Carbonates observed in CI and CM chondrites include breunnerite $(Mg,Fe)CO_3$, and less frequently calcite $CaCO_3$, and dolomite $CaMg(CO_3)_2$. The carbonate abundances range are about 0.05 – 0.5% by mass. Whewellite is a trace phase observed in Murchison. The CI and CM chondrites contain more presolar grains than other meteorites, mainly presolar diamonds. The presolar grain inventories in CI chondrites are 10 μg/g graphite, 14 μg/g SiC, and 940 – 1400 μg/g diamonds. The inventories in CM chondrites are 5 – 6 μg/g graphite, 4 –

14 μg/g SiC, and 400 – 740 μg/g diamonds. Carbon dissolved in metal is insignificant because metal is absent in CI chondrites and a minor phase in CM chondrites.

The CI chondrites contain 27 – 44.3 mg/g carbon with an average value of 35.18 mg/g [2]. Much of this carbon is in organic material. For example, Briggs and Mamikunian [78] estimate 54 mg/g, 62 mg/g, and 96 mg/g organic matter containing about 50% carbon in the Tonk, Orgueil, and Ivuna CI chondrites. About 25 – 30% of the organics in CI chondrites are soluble and the remaining 75 – 70% is an insoluble aromatic polymer. Hayes [79] gives the elemental composition of the organic polymer in the Orgueil CI chondrite as $C_{100}H_{72}N_2O_{10}S_4$, corresponding to about 75% carbon, 10% oxygen, 8% sulfur, 5% hydrogen, and 2% nitrogen. Remusat et al. [89] give a slightly different formula of $C_{100}H_{72}N_3O_{22}S_{4.5}$ for the polymer in Orgueil and Murchison. Hayatsu et al. [90] give a similar formula $C_{100}H_{70}N_{2.5}O_{12}S_2$ for the polymer in Murchison. The structure of the polymer is complex and not fully known. Briggs and Mamikunian [78] describe the aromatic polymer as similar to humic acids in soils. Other workers compare the polymer to terrestrial coals. The work of Remusat et al. [89] gives a picture of the molecular structure of the polymer (their Figure 4). This shows small polyaromatic hydrocarbons (2 – 6 rings) linked together with aliphatic chains. The polymer also contains nitrogen (pyrrole) and sulfur (thiophene) heterocyclic rings and oxygen in ether (C-O-C) and ester (C=O) bonds.

Much of the work on soluble organic compounds is for the Murchison meteorite because 100 kg of this CM chondrite is available for study. Prior to its fall in 1969, the Orgueil meteorite was the most studied carbonaceous chondrite. However, much of this

earlier work on soluble organics is wrong because terrestrial contamination affected the results. Thus, Briggs and Mamikunian [78] state that alkanes are abundant soluble organics, while we now know that these were terrestrial contaminants. The soluble organic material in Murchison is a mixture of a large number of compounds including carboxylic acids, amino acids, sugars, nitrogen-bearing heterocyclic compounds, amines, sulfur-bearing heterocyclics, aliphatic and aromatic hydrocarbons, and alkyl phosphonic acids [91]. Carboxylic acids with 2 – 5 carbon atoms are the most abundant soluble organics (~ 300 μg/g). Their characteristics such as an equal abundance of straight chain and branched structural isomers, decreasing abundance with higher carbon number, and lack of chirality show they are abiotic. The amino acids include 8 of the 20 amino acids found in proteins and other unique to meteorites. Their characteristics also indicate an abiotic origin (decreasing abundance with increasing molecular weight, diverse structures, unique molecular configurations). However, both the amino acids found in proteins and those that are not, display a small excess of the L forms instead of equal amounts of L and D forms [91]. This is not evidence of a biological origin because chiral abiotic synthesis of organic molecules is commonplace, e.g., for pharmaceuticals. The soluble organics in Murchison plausibly originated during aqueous alteration reactions on the meteorite parent body. Outgassing of CM chondrites produces a H_2O (73%) - CO_2 (19%) - H_2 (2.7%) - H_2S (2.3%) - CO (1.8%) vapor that gives abundant liquid water upon cooling. About 3 ppmv NH_3 also are produced [92]. Hydrous minerals, carbonates, and organics probably formed during and/or after these outgassing reactions.

Finally, earlier in section 3, we discussed the tar line in the solar nebula. This is where the polymeric organic material in carbonaceous chondrites forms (or decomposes) in the solar nebula. Nakano et al. [93] showed that two types of analog materials to interstellar organic material vaporized at temperatures above 350 K or 450 K. In their nebular thermal model these temperatures corresponded to 2.7 astronomical units (AU) or 2.1 AU. At earlier times, when the nebula was hotter, the tar line was further out. The model of Lodders [26] places the tar line at Jupiter's orbit where it provides the glue for runaway accretion of Jupiter during its formation. There are large amounts of polymeric organic matter like that in carbonaceous chondrites in the outer solar system, e.g., see the review by Prinn and Fegley [43]. This indicates that the “glue” necessary for Jupiter's formation was readily available.

10. References

1. K. Lodders and B. Fegley, Jr., *Chemistry of the Solar System*, Royal Society of London, London (2008).
2. K. Lodders, Astrophys. J. **591**, 1220 (2003).
3. K. Lodders, Astrophys. J. **674**, 607 (2008).
4. V. M. Goldschmidt, *Geochemische Verteilungsgesetze det Elemente*, J. Dybwad, Oslo (1937).
5. V. M. Goldschmidt, *Geochemistry*, Clarendon Press, Oxford (1954).
6. H. E. Suess, Z. Naturforsch. **2a**, 311 (1947).
7. H. E. Suess, Z. Naturforsch. **2a**, 604 (1947).
8. H. Brown and E. Goldberg, Phys. Rev. **76**, 1260 (1949).
9. H. Brown, Rev. Modern Phys. **21**, 625 (1949).
10. H. E. Suess and H. C. Urey, Rev. Mod. Phys. **28**, 53 (1956).
11. E. M. Burbidge, G. R. Burbidge, W. A. Fowler, and F. Hoyle, Rev. Mod. Phys. **29**, 547 (1957).
12. A. G. W. Cameron, Publ. Astron. Soc. Pacific **69**, 201 (1957).
13. B. Mason, *Handbook of Elemental Abundances in Meteorites*, Gordon and Breach, New York (1971).
14. B. Mason, in *Data of Geochemistry, Sixth Edition* edited M. Fleischer, U.S. Govt. Print. Office, Washington, D.C. (1979).
15. E. Anders and M. Ebihara, Geochim. Cosmochim. Acta **46**, 2363 (1982).

16. E. Anders and N. Grevesse, Geochim. Cosmochim. Acta **53**, 197 (1989).
17. A. G. W. Cameron, in *Essays in Nuclear Astrophysics* edited C. A. Barnes, D. D. Clayton, and D. N. Schramm, Cambridge University Press, Cambridge, (1982), p. 23.
18. K. Lodders and B. Fegley, Jr., *The Planetary Scientist's Companion*, Oxford Univ. Press, New York (1998).
19. K. Lodders and B. Fegley, Jr., Icarus **155**, 393 (2002).
20. J. W. Larimer, Geochim. Cosmochim. Acta **39**, 389 (1975).
21. J. W. Larimer and M. Bartholomay, Geochim. Cosmochim. Acta **43**, 1453 (1979).
22. A. N. Krot, B. Fegley, Jr., K. Lodders, and H. Palme, in *Protostars and Planets IV*, edited V. Mannings, A. P. Boss, and S. S. Russell, University of Arizona Press, Tucson (2000), p. 1019.
23. J. S. Lewis and R. G. Prinn, Astrophys. J. **238**, 357 (1980).
24. B. Fegley, Jr., in *Workshop on the Origins of Solar Systems* edited J. A. Nuth and P. Sylvester, LPI, Houston (1988), Tech. Rep. No. 88-04, p. 51.
25. A. G. W. Cameron, Meteoritics **30**, 133 (1995).
26. K. Lodders, Astrophys. J. **611**, 587 (2004).
27. T. D. Jones, L. A. Lebofsky, J. S. Lewis, and M. S. Marley, Icarus **88**, 172 (1990).
28. W. M. Irvine and R. F. Knacke, in *The Origin and Evolution of Planetary and Satellite Atmospheres* edited S. K. Atreya, J. B. Pollack, and M. S. Matthews, Univ. Arizona Press, Tucson (1989) p. 3.
29. A. Omont, in *Chemistry in Space* edited J. M. Greenberg and V. Pirronello, Kluwer Academic Publishers, Dordrecht, Netherlands (1991), p. 171.
30. A. Omont, Rep. Prog. Phys. **70**, 1099 (2007).
31. G. R. Huss, A. J. Fahey, R. Gallino, G. J. Wasserburg, Astrophys. J. **430**, L81 (1994).
32. I.D. Hutcheon, G. R. Huss, A. J. Fahey, G. J. Wasserburg, Astrophys. J. **425**, L97 (1994).
33. L. R. Nittler, C. M. O.'D. Alexander, X. Gao, R. M. Walker, and E. K. Zinner, Nature **370**, 443 (1994).
34. L. R. Nittler, C. M. O'.D. Alexander, X. Gao, R. M. Walker, and E. Zinner, Astrophys. J. **483**, 475 (1997).
35. L. R. Nittler, C. M. O'.D. Alexander, J. Wang, and X. Gao, Nature 393, 222 (1998).
36. L. R. Nittler, and C. M. O'.D. Alexander, Lunar Planet. Sci. **30**, abstract #2041 (1999).
37. B.-G. Choi, G. R. Huss, G. J. Wasserburg, and R. Gallino, Science **282**, 1284 (1998).
38. B. G. Choi, G. J. Wasserburg, and G. R. Huss, Astrophys. J. **522**, L133 (1999).
39. N. Krestina, W. Hsu, and G. J. Wasserburg, Lunar Planet. Sci. **33**, abstract 1425 (2002).
40. A. N. Nguyen and E. Zinner, Science **303**, 1496 (2004).
41. T. Bernatowicz, S. Amarai, E. K. Zinner and R. S. Lewis, Astrophys. J. **373**, L73 (1991).

42. K. Lodders and S. Amari, Chemie der Erde **65**, 93 (2005).
43. R. G. Prinn and B. Fegley, Jr., in *Origin and Evolution of Planetary and Satellite Atmospheres*, edited S. K. Atreya, J. B. Pollack, M. S. Matthews, University of Arizona Press, Tucson, AZ (1989), p. 78.
44. B. Fegley, Jr., in *Encyclopedia of Planetary Sciences*, edited J. H. Shirley and R. W. Fairbanks, Chapman and Hall, London (1997), p. 169.
45. K. Lodders and B. Fegley, Jr., Earth Planet. Sci. Lett. **117**, 125 (1993).
46. K. Lodders and B. Fegley, Jr., Meteoritics **30**, 661 (1995).
47. K. Lodders and B. Fegley, Jr., in *Astrophysical Implications of the Laboratory Study of Presolar Materials* edited T. J. Bernatowicz and E. Zinner, AIP Conference Proceedings 402, American Institute of Physics, Woodbury, NY (1997), p. 279.
48. B. Fegley, Jr. and K. Lodders, Icarus **110**, 117 (1994).
49. G. N. Lewis and M. Randall, *Thermodynamics*, McGraw-Hill, New York (1961).
50. H. Palme and B. Fegley, Jr., Earth Planet. Sci. Lett. **101**, 180 (1990).
51. J. S. Lewis, Science **136**, 440 (1974).
52. B. Fegley, Jr. and H. Palme, Earth Planet. Sci. Lett. **72**, 311 (1985).
53. A. S. Kornacki and B. Fegley, Jr., Earth Planet. Sci. Lett. **79**, 217 (1986).
54. B. Fegley, Jr., in *The Chemistry of Life's Origins* edited J. M. Greenberg et al., Kluwer Academic Publishers, Netherlands (1993), p. 75.
55. H. Palme and F. Wlotzka, Earth Planet. Sci. Lett. **33**, 45 (1976).
56. A. El Goresy, K. Nagel, and P. Ramdohr, Proc. Lunar Planet. Sci. Conf. **9**, 1279 (1978).
57. B. Fegley, Jr. and A. S. Kornacki, Earth Planet. Sci. Lett. **68**, 181 (1984).
58. A. Bischoff and H. Palme, Geochim. Cosmochim. Acta **51**, 2733 (1987).
59. J. D. Blum, G. J. Wasserburg, I. D. Hutcheon, J. R. Beckett, and E. M. Stolper, Nature **331**, 405 (1988).
60. J. W. Larimer, Geochim. Cosmochim. Acta **31**, 1215 (1967).
61. L. Grossman and J. W. Larimer, Rev. Geophys. Space Phys. **12**, 71 (1974).
62. B. Fegley, Jr. and J. S. Lewis, Icarus **41**, 439 (1980).
63. J. W. Larimer, Geochim. Cosmochim. Acta **37**, 1603 (1973).
64. J. S. Lewis, Earth Planet. Sci. Lett. **15**, 286 (1972).
65. D. L. Baulch, D. D. Drysdale, J. Duxbury, and S. J. Grant, *Evaluated Kinetic Data for High Temperature Reactions*, Butterworths, London (1976).
66. J. S. Lewis, S. S. Barshay, and B. Noyes, Icarus **37**, 190 (1979).
67. L. Schaefer and B. Fegley, Jr., Icarus **186**, 462 (2007).
68. E. Anders, R. Hayatsu, and M. H. Studier, Science **182**, 781 (1973).
69. S. Miller, J Am Chem Soc **77**, 2351, (1955).
70. H. C. Urey, in *Thirteenth International Congress: Pure and Applied Chemistry and Plenary Lectures*, Almquist and Wiksells, Stockholm, Sweden (1953), pp. 188.
71. A. E. Glassgold, Ann. Rev. Astron. Astrophys. **34**, 241(1996).
72. M. E. Dry, in *Catalysis Science and Technology Vol. 1*, edited. J. R. Anderson and M. Boudart, Springer Verlag, Berlin (1981), p. 159.

73. H. J. Krebs, H. P. Bonzel, and G. Gafner, Surface Sci. **88**, 269 (1979).
74. M. A. Vannice, in *Catalysis Science and Technology Vol. 3*, edited J. R. Anderson and M. Boudart, Springer Verlag, Berlin (1982), p. 139.
75. B. Fegley, Jr. and Y. Hong, EOS Trans AGU **79**, S361 (1998).
76. J. P. Bradley, D. E. Brownlee, and P. Fraundorf, Science **233**, 56 (1984).
77. J. P. Bradley and D. E. Brownlee, Science **231**, 1542 (1986).
78. M. H. Briggs and G. Mamikunian, Space Sci. Rev. **1**, 647 (1963).
79. J. M. Hayes, Geochim. Cosmochim. Acta **31**, 1395 (1967).
80. R. Hayatsu and E. Anders, Topics Current Chem. **99**, 1 (1981).
81. J. Llorca and I. Casanova, Meteoritics Planet. Sci. **33**, 243 (1998).
82. J. Koblitz, METBASE Version 7.1 for Windows (2005).
83. C. C. Kung and R. N. Clayton, Earth Planet Sci. Lett. **38**, 421 (1978).
84. C. M. O'D. Alexander, P. Swan, and C. Prombo, Meteoritics Planet. Sci. **29**, 79 (1994).
85. S. S. Russell, M. R. Lee, J. W. Arden, and C. T. Pillinger, Meteoritics Planet. Sci. **30**, 399 (1995).
86. A. Bischoff, T. Grund, T. Jording, B. Heying, R. D. Hoffmann, U. C. Rodewald, and R. Pöttgen, Meteoritics Planet Sci. **40**, 5043 (2005).
87. J. M. Hayes and K. Biemann, Geochim. Cosmochim. Acta **32**, 239 (1967).
88. K. Hashizume and N. Sugiura, Geochim. Cosmochim. Acta **61**, 859 (1997).
89. L. Remusat, F. Robert, and S. Derenne, C. R. Geoscience **339**, 895 (2007).
90. R. Hayatsu, R. E. Winans, R. G. Scott, R. L. McBeth, L. P. Moore, and M. H. Studier, Science **207**, 1202 (1980).
91. M. A. Sephton, Phil. Trans. Roy. Soc. A, **363**, 2729 (2005).
92. B. Fegley, Jr. and L. Schaefer, Meteoritics Planet. Sci. **43**, A42 (2008).
93. H. Nakano, A. Kouchi, S. Tachibana, and A. Tsuchiyama, Astrophys. J. **592**, 1252 (2003).

Table Captions

Table 1. Protosolar elemental abundances. Elemental abundances are given on the cosmochemical scale (normalized to 10^6 atoms of Si). Abundances of radioactive elements designated with an asterix are abundances at 4.55×10^9 years ago. Abundances are taken from K. Lodders, Ap. J., 591, 1220-1247, 2003 and K. Lodders, Ap. J., 674, 607-611, 2008.

Table 2. Common presolar dust grains and their possible fate(s) in the solar nebula (e.g., destruction by reactions with solar nebula material, or possible preservation sites).

Table 3. Interstellar gas molecules and their possible fate(s) in the solar nebula (e.g., destruction by reactions with solar nebula material, or possible preservation sites).

Table 4. Equilibrium condensation of the elements in a gas of protosolar composition at 10^{-4} bar total pressure. Abbreviations: At. No. = atomic number, El. = element, T_C (K) = condensation temperature in Kelvins, 50% T_C = temperature at which 50% of the element is condensed. Notes: A = atmophile, HV = highly volatile, ME = major element, MV = moderately volatile, RL = refractory lithophile, RS = refractory siderophile.

Table 5. Carbon depletions in chondritic meteorites relative to the protosolar carbon abundance. Meteorite abundances are average values for the given meteorite type. Ratios are by mass. The $(C/Si)_{solar}$ ratio is taken from Table 1.

Table 6. Nitrogen depletions in chondritic meteorites relative to the protosolar nitrogen abundance. Meteorite abundances are average values for the given meteorite type. Ratios are by mass. The $(N/Si)_{solar}$ ratio is taken from Table 1.

Table 1

Atomic Number	Element Name	Chemical Symbol	Atomic Abundance
1	Hydrogen	H	2.431×10^{10}
2	Helium	He	2.343×10^{9}
3	Lithium	Li	55.47
4	Beryllium	Be	0.7374
5	Boron	B	17.32
6	Carbon	C	7.079×10^{6}
7	Nitrogen	N	1.950×10^{6}
8	Oxygen	O	1.413×10^{7}
9	Fluorine	F	841.1
10	Neon	Ne	2.148×10^{6}
11	Sodium	Na	5.751×10^{4}
12	Magnesium	Mg	1.020×10^{6}
13	Aluminum	Al	8.410×10^{4}
14	Silicon	Si	$\equiv1.00\times10^{6}$
15	Phosphorus	P	8373
16	Sulfur	S	4.449×10^{5}
17	Chlorine	Cl	5237
18	Argon	Ar	9.032×10^{4}
19	Potassium	K	3692
			3697*
20	Calcium	Ca	6.287×10^{4}
21	Scandium	Sc	34.20
22	Titanium	Ti	2422
23	Vanadium	V	288.4
24	Chromium	Cr	1.286×10^{4}
25	Manganese	Mn	9168
26	Iron	Fe	8.380×10^{5}
27	Cobalt	Co	2323
28	Nickel	Ni	4.780×10^{4}
29	Copper	Cu	527.0
30	Zinc	Zn	1226
31	Gallium	Ga	35.97
32	Germanium	Ge	120.6
33	Arsenic	As	6.089
34	Selenium	Se	65.79
35	Bromine	Br	11.32
36	Krypton	Kr	55.15
37	Rubidium	Rb	6.572
			6.694*
38	Strontium	Sr	23.64
			23.52*
39	Yttrium	Y	4.608

Table 1 Cont'd

Atomic Number	Element Name	Chemical Symbol	Atomic Abundance
40	Zirconium	Zr	11.33
41	Niobium	Nb	0.7554
42	Molybdenum	Mo	2.601
44	Ruthenium	Ru	1.900
45	Rhodium	Rh	0.3708
46	Palladium	Pd	1.435
47	Silver	Ag	0.4913
48	Cadmium	Cd	1.584
49	Indium	In	0.1810
50	Tin	Sn	3.733
51	Antimony	Sb	0.3292
52	Tellurium	Te	4.815
53	Iodine	I	0.9975
54	Xenon	Xe	5.391
55	Cesium	Cs	0.3671
56	Barium	Ba	4.351
57	Lanthanum	La	0.4405
58	Cerium	Ce	1.169
59	Praseodymium	Pr	0.1737
60	Neodymium	Nd	0.8355
			0.8343*
62	Samarium	Sm	0.2542
			0.2554*
63	Europium	Eu	0.09513
64	Gadolinium	Gd	0.3321
65	Terbium	Tb	0.05907
66	Dysprosium	Dy	0.3862
67	Holmium	Ho	0.08986
68	Erbium	Er	0.2554
69	Thulium	Tm	0.03700
70	Ytterbium	Yb	0.2484
71	Lutetium	Lu	0.03572
			0.03580*
72	Hafnium	Hf	0.1699
			0.1698*
73	Tantalum	Ta	0.02099
74	Tungsten	W	0.1277
75	Rhenium	Re	0.05254
			0.05509*
76	Osmium	Os	0.6738
			0.6713*
77	Iridium	Ir	0.6488

Table 1 Cont'd

Atomic Number	Element Name	Chemical Symbol	Atomic Abundance
78	Platinum	Pt	1.357
79	Gold	Au	0.1955
80	Mercury	Hg	0.4128
81	Thallium	Tl	0.1845
82	Lead	Pb	3.258
			3.234*
83	Bismuth	Bi	0.1388
90	Thorium	Th	0.03512
			0.04399*
92	Uranium	U	9.306×10^{-3}
			24.631×10^{-3}*

Table 2. Presolar Dust Grains

Component	Reactions	Preservation Site(s)
Silicates (olivine and pyroxene)	Amorphous material will be annealed and equilibrated, crystalline material altered by metamorphism and chemical (e.g., aqueous) processing	Low T meteorite matrices, IDPs, identified by O-isotopes
Diamond	Oxidized during parent body metamorphism	Chondrite matrices, identified by anomalous noble gas component
Graphite	Oxidized at high T to form CO, hydrogenated at low T to form CH_4	Primitive meteorite matrices, identified by anomalous noble gas component
Polycyclic Aromatic Hydrocarbons (PAHs)	Oxidized at high T to form CO + H_2, isotopic equilibration with nebular vapor, partial pyrolysis to more C-rich matter	D-rich organics observed in low T meteorite matrices and interplanetary dust particles, not conclusively identified as PAHs
Icy Grain Mantles	Evaporation of ices, chemical and isotopic equilibration with nebular gas, photolysis in outer nebula	Comets and other icy bodies in outer solar nebula?
SiC	Oxidation (e.g., by O, OH, H_2O) to silica and eventually silicates	Circumstellar SiC grains observed in primitive meteorites
Hibonite ($CaAl_{12}O_{19}$)	Crystalline material altered by metamorphic processing	Low T meteorite matrices; identified by O-isotope
TiO_2	Crystalline material altered by metamorphic processing	Low T meteorite matrices; identified by O-isotope
Corundum (Al_2O_3)	Crystalline material altered by metamorphic processing	Low T meteorite matrices; identified by O-isotope
TiC	Oxidation to TiO_2 and eventually titanates	Observed inside presolar graphite grains in meteorites
Spinel ($MgAl_2O_4$)	Crystalline material altered by metamorphic processing	Low T meteorite matrices; identified by O-isotope
MgS	Oxidation (e.g., by O, OH, H_2O) to Mg oxides and silicates	Low T meteorite matrices? Sensitive to water and O_2

Table 3. Interstellar Gas Molecules

Molecule(s)	Nebular Processing	Possible Preservation Site(s)
CO	Also stable high T form of C in nebula, use C & O isotopes to distinguish nebular from interstellar CO?	Trapped in clathrate hydrate or condensed as CO ice in comets or other icy bodies in outermost nebula
N_2	Also stable high T form of N in nebula, use N isotopes to distinguish nebular from interstellar N_2?	Trapped in clathrate hydrate or condensed as N_2 ice in comets or other icy bodies in outermost nebula
HDO	Isotopic exchange equilibrates D/H with nebular H_2 at sufficiently high temperatures in inner nebula	HDO ice in comets & icy satellites, HDO in hydrated silicates on asteroids?
HCN	Also produced by shock chemistry in solar nebula & Jovian protoplanetary subnebulae, use isotopes to distinguish source?	HCN ice in comets and outer nebula bodies?, conversion to organic matter on meteorite parent bodies
H_2CO	Thermal decomposition and/or photolysis to H_2 + CO, polymerization to POM?	H_2CO & POM observed in comets
CH_3OH	Pyrolized to CO + H_2	Cometary ices
CH_3CN	Thermal decomposition	Cometary ices
SO_2	Reduction to H_2S + H_2O at high temperatures	Cometary ices
COS	Thermal decomposition and/or photolysis to CO + S, subsequent conversion of S to H_2S	Cometary ices
H_2S	Also stable high T form of S in nebula	Cometary ices, probably difficult to distinguish from nebular H_2S
H_2CS	Thermal decomposition to CO + H_2S in fairly low temperatures in nebula	Cometary ices

Table 5. Carbon in Chondritic Meteorites

Meteorite	C (mg/g)	Si (mg/g)	$(C/Si)_{meteorite}$	$\frac{(C/Si)_{meteorite}}{(C/Si)_{solar}} \times 100$
CI	34.800	105.700	0.3292	10.8744
CM	19.300	136.475	0.1414	4.6708
CV	2.550	158.414	0.0161	0.5318
H	1.215	170.600	0.0071	0.2345
L	1.640	185.267	0.0089	0.2940
LL	2.350	188.673	0.0125	0.4129
EH	3.575	165.456	0.0216	0.7315
EL	4.283	184.620	0.0232	0.7664

Table 6. Nitrogen in Chondritic Meteorites

Meteorite	N (mg/g)	Si (mg/g)	$(N/Si)_{meteorite}$	$\frac{(N/Si)_{meteorite}}{(N/Si)_{solar}} \times 100$
CI	2.948	105.700	0.0279	2.8676
CM	1.255	136.475	0.0092	0.9455
CV	0.413	158.414	0.0026	0.2681
H	0.034	170.600	2×10^{-4}	0.0205
L	0.034	185.267	2×10^{-4}	0.0189
LL	0.050	188.673	3×10^{-4}	0.0272
EH	0.300	165.456	0.0018	0.1864
EL	0.240	184.620	0.0013	0.1337

Table 4.

At. No.	El.	T_C (K)	Initial Condensate {Dissolving Species}	50% T_C (K)	Major gases	Major phases/hosts	Notes
1	H	182	H_2O ice	—	H_2	—	A
2	He	<3	He ice	—	He	—	A
3	Li	—	{Li_4SiO_4, Li_2SiO_3}	1142	LiCl, LiF	Forsterite + enstatite	MV
4	Be	—	{$BeCa_2Si_2O_7$}	1452	Be, $Be(OH)_2$, BeOH	Melilite	RL
5	B	—	{$CaB_2Si_2O_8$}	908	HBO, HBO_2, $NaBO_2$	Feldspar	MV
6	C	78	$CH_4 \cdot 7H_2O$	40	CO, CH_4	$CH_4 \cdot 7H_2O$ + CH_4 ice	A
7	N	131	$NH_3 \cdot H_2O$	123	N_2, NH_3	$NH_3 \cdot H_2O$	A
8	O	182	H_2O ice[a]	180	CO, H_2O	Rock + H_2O ice	A
9	F	739	$Ca_5[PO_4]_3F$	734	HF	F apatite	MV
10	Ne	9.3	Ne ice	9.1	Ne	Ne ice	A
11	Na	—	{$NaAlSi_3O_8$}	958	Na, NaCl	Feldspar	MV
12	Mg	1397	Spinel	—	Mg		ME
		1354	Forsterite[b]	1336		Forsterite	
13	Al	1677	Al_2O_3	1653	Al, AlOH, Al_2O, AlS, AlH, AlO	Hibonite	RL
14	Si	1529	Gehlenite	—	SiO,SiS		ME
		1354	Forsterite[b]	1310		Forsterite + enstatite	
15	P	1248	Fe_3P	1229	PO, P, PN, PS	Schreibersite	MV
16	S	704	FeS	664	H_2S,HS	Troilite	MV
17	Cl	954	$Na_4[Al_3Si_3O_{12}]Cl$	948	HCl, NaCl, KCl	Sodalite	MV
18	Ar	48	$Ar \cdot 6H_2O$	47	Ar	$Ar \cdot 6H_2O$	A
19	K	—	{$KAlSi_3O_8$}	1006	K, KCl, KOH	Feldspar	MV
20	Ca	1659	$CaAl_{12}O_{19}$	1517	Ca	Hibonite + gehlenite	RL
21	Sc	—	{Sc_2O_3}	1659	ScO	Hibonite	RL
22	Ti	1593	$CaTiO_3$	1582	TiO, TiO_2	Titanate	RL
23	V	—	{VO,V_2O_3}	1429	VO_2, VO	Titanate	RL
24	Cr	—	{Cr}	1296	Cr	Fe alloy	MV
25	Mn	—	{Mn_2SiO_4, $MnSiO_3$}	1158	Mn	Forsterite + enstatite	MV

Table 4 Cont'd

At. No.	El.	T_C (K)	Initial Condensate {Dissolving Species}	50% T_C (K)	Major gases	Major phases/hosts	Notes
26	Fe	1357[c]	Fe metal[c]	1334	Fe	Fe alloy	ME
27	Co	—	{Co}	1352	Co	Fe alloy	RS
28	Ni	—	{Ni}	1353	Ni	Fe alloy	RS
29	Cu	—	{Cu}	1037	Cu	Fe alloy	MV
30	Zn	—	{Zn_2SiO_4, $ZnSiO_3$}	726	Zn	Forsterite + enstatite	MV
31	Ga	—	{Ga,Ga_2O_3}	968	GaOH, GaCl	Fe alloy + feldspar	MV
32	Ge	—	{Ge}	883	GeS, GeSe	Fe alloy	MV
33	As	—	{As}	1065	As	Fe alloy	MV
34	Se	—	{$FeSe_{0.96}$}[d]	697	H_2Se, GeSe	Troilite	MV
35	Br	—	{$CaBr_2$}	546	HBr, NaBr	Cl apatite	HV
36	Kr	53	Kr·$6H_2O$	52	Kr	Kr·$6H_2O$	A
37	Rb	—	{Rb silicate}	800	Rb, RbCl	Feldspar	MV
38	Sr	—	{$SrTiO_3$}	1464	Sr, $SrCl_2$, $Sr(OH)_2$, SrOH	Titanate	RL
39	Y	—	{Y_2O_3}	1659	YO	Hibonite	RL
40	Zr	1764	ZrO_2	1741	ZrO_2, ZrO	ZrO_2	RL
41	Nb	—	{NbO,NbO_2}	1559	NbO_2, NbO	Titanate	RL
42	Mo	—	{Mo}	1590	MoO, Mo, MoO_2	Refractory metal alloy	RS
44	Ru	—	{Ru}	1551	Ru	Refractory metal alloy	RS
45	Rh	—	{Rh}	1392	Rh	Refractory metal alloy	RS
46	Pd	—	{Pd}	1324	Pd	Fe alloy	MV
47	Ag	—	{Ag}	996	Ag	Fe alloy	MV
48	Cd	—	{$CdSiO_3$, CdS}	652	Cd	Enstatite + troilite	HV
49	In	—	{InS, InSe, InTe}	536	In, InCl, InOH	FeS	HV
50	Sn	—	{Sn}	704	SnS, SnSe	Fe alloy	MV
51	Sb	—	{Sb}	979	SbS, Sb	Fe alloy	MV
52	Te	—	{Te}	709	Te, H_2Te	Fe alloy	MV
53	I	—	{CaI_2}	535	I, HI	Cl apatite	MV/HV?

Table 4 Cont'd

At. No.	El.	T_C (K)	Initial Condensate {Dissolving Species}	50% T_C (K)	Major gases	Major phases/hosts	Notes
54	Xe	69	$Xe{\cdot}6H_2O$	68	Xe	$Xe{\cdot}6H_2O$	A
55	Cs	—	{Cs silicate}	799	CsCl, Cs, CsOH	Feldspar	MV/HV?
56	Ba	—	$\{BaTiO_3\}$	1455	$Ba(OH)_2$, BaOH, BaS, BaO	Titanate	RL
57	La	—	$\{La_2O_3\}$	1578	LaO	Hibonite + titanate	RL
58	Ce	—	$\{CeO_2,Ce_2O_3\}$	1478	CeO_2, CeO	Hibonite + titanate	RL
59	Pr	—	$\{Pr_2O_3\}$	1582	PrO	Hibonite + titanate	RL
60	Nd	—	$\{Nd_2O_3\}$	1602	NdO	Hibonite	RL
62	Sm	—	$\{Sm_2O_3\}$	1590	SmO, Sm	Hibonite + titanate	RL
63	Eu	—	$\{EuO, Eu_2O_3\}$	1356	Eu	Hibonite + titanate + feldspar	RL
64	Gd	—	$\{Gd_2O_3\}$	1659	GdO	Hibonite	RL
65	Tb	—	$\{Tb_2O_3\}$	1659	TbO	Hibonite	RL
66	Dy	—	$\{Dy_2O_3\}$	1659	DyO, Dy	Hibonite	RL
67	Ho	—	$\{Ho_2O_3\}$	1659	HoO, Ho	Hibonite	RL
68	Er	—	$\{Er_2O_3\}$	1659	ErO, Er	Hibonite	RL
69	Tm	—	$\{Tm_2O_3\}$	1659	Tm, TmO	Hibonite	RL
70	Yb	—	$\{Yb_2O_3\}$	1487	Yb	Hibonite + titanate	RL
71	Lu	—	$\{Lu_2O_3\}$	1659	LuO	Hibonite	RL
72	Hf	1703	HfO_2	1684	HfO	HfO_2	RL
73	Ta	—	$\{Ta_2O_5\}$	1573	TaO_2, TaO	Hibonite + titanate	RL
74	W	—	{W}	1789	WO, WO_2, WO_3	Refractory metal alloy	RS
75	Re	—	{Re}	1821	Re	Refractory metal alloy	RS
76	Os	—	{Os}	1812	Os	Refractory metal alloy	RS
77	Ir	—	{Ir}	1603	Ir	Refractory metal alloy	RS
78	Pt	—	{Pt}	1408	Pt	Refractory metal alloy	RS
79	Au	—	{Au}	1060	Au	Fe alloy	MV
80	Hg	—	{HgS, HgSe, HgTe}	252	Hg	Troilite	MV/HV?

Table 4 Cont'd

At. No.	El.	T_C (K)	Initial Condensate {Dissolving Species}	50% T_C (K)	Major gases	Major phases/hosts	Notes
81	Tl	—	{Tl_2S, Tl_2Se, Tl_2Te}	532	Tl	Troilite	HV
82	Pb	—	{Pb}	727	Pb, PbS	Fe alloy	HV
83	Bi	—	{Bi}	746	Bi	Fe alloy	HV
90	Th	—	{ThO_2}	1659	ThO_2	Hibonite	RL
92	U	—	{UO_2}	1610	UO_2	Hibonite	RL

[a]22.75% of oxygen is condensed into rock before water ice condensation. [b]Major condensed reservoir of element. [c]Condensation temperature of pure iron metal. [d]Modeling assumes solution of $FeSe_{0.96}$ for which reliable thermodynamic properties exist, instead of FeSe.

Figure Captions

Figure 1. Schematic diagram comparing three different models for the pressure and temperature profile of the solar nebula as a function of radial distance. The pressure and temperature profiles are taken from J. S. Lewis, Science, 186, 440, 1974; A. G. W. Cameron, Meteoritics, 30, 133, 1995; K. Willacy et al., Astron. Astrophys. 338, 995, 1998.

Figure 2. Chemistry of sulfur in the solar nebula as a function of pressure and temperature, shown as cumulative percent of total sulfur. The species S, HS, H_2S, and SiS are gas species, and FeS (troilite) is a condensed phase. The calculations were done for the pressure and temperature profile of J. S. Lewis, Science, 186, 440, 1974.

Figure 3. Gas phase chemistry of sulfur in the solar nebula as a function of temperature at a constant pressure of 10^{-4} bar. Abundances are given in $\log_{10} X_i$ (mole fraction).

Figure 4. Condensation chemistry in the solar nebula as a function of temperature and pressure. The dashed line is the pressure and temperature profile of J. S. Lewis, Science, 186, 440, 1974.

Figure 5. Chemistry of phosphorus in the solar nebula as a function of pressure and temperature, shown as cumulative percent of total phosphorus. The species P, PN, PO, PH, PS, PH_2, and P_2 are gas species. Schreibersite, whitlockite, hydroxyapatite, and fluorapatite are condensed phases. The calculations were done for the pressure and temperature profile of J. S. Lewis, Science, 186, 440, 1974.

Figure 6. Major carbon and nitrogen gases in the solar nebula as a function of temperature and pressure. The lines show where the gases have equal abundance (i.e. where CO = CH_4 and where N_2 = NH_3).

Figure 7. Gas phase chemistry of carbon in the solar nebula as a function of temperature at a constant pressure of 10^{-4} bar. Abundances are given in cumulative % of total carbon.

Figure 8. Gas phase chemistry of carbon in the solar nebula as a function of temperature at a constant pressure of 10^{-4} bar. Abundances are given in $\log_{10} X_i$ (mole fraction).

Figure 9. Gas phase chemistry of nitrogen in the solar nebula as a function of temperature at a constant pressure of 10^{-4} bar. Abundances are given in cumulative % of total nitrogen.

Figure 10. Gas phase chemistry of nitrogen in the solar nebula as a function of temperature at a constant pressure of 10^{-4} bar. Abundances are given in $\log_{10} X_i$ (mole fraction).

Figure 11. Comparison of methane production yields from different types of catalysts as a function of temperature. The catalysts include a control (empty boat), filings of the Gibeon (iron) meteorite, Fe metal powder, the Gao H5 chondrite, and terrestrial olivine (green sand from Hawaii).

Figure 12. Comparison of methane production yields at 800 K for different types of catalysts as a function of surface area (ppmv CH_4 produced/mm^2). The catalysts include the Gao H5 meteorite, terrestrial olivine, the Gibeon (iron) meteorite, Pt metal, and Fe metal.

Figure 13. Methane produced by the commercial NH_3 synthesis catalyst KM1R as a function of time.

Figure 14. Methane produced from catalysis by terrestrial magnetite extracted from green Hawaiian sand as a function of time.

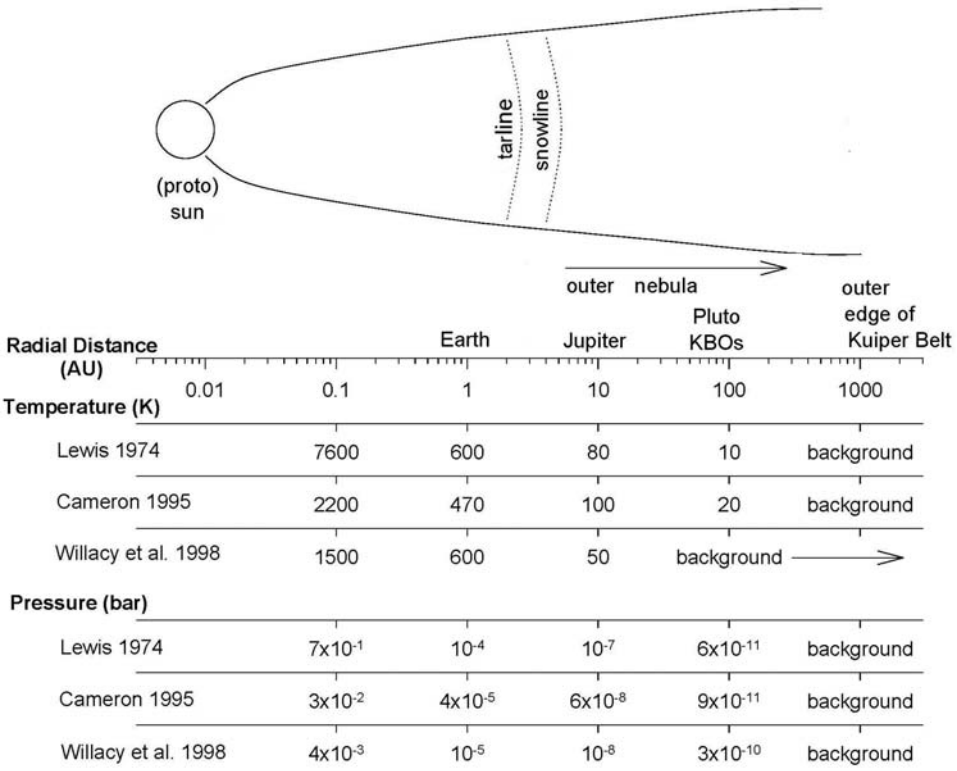
tarline
snowline
(proto)
sun
outer nebula
outer
edge of
Kuiper Belt
Pluto
KBOs
Earth
Jupiter
Radial Distance
(AU)
0.01
0.1
1
10
100
1000
Temperature (K)
Lewis 1974
7600
600
80
10
background
Cameron 1995
2200
470
100
20
background
Willacy et al. 1998
1500
600
50
background
Pressure (bar)
Lewis 1974
7x10-1
10-4
10-7
6x10-11
background
Cameron 1995
3x10-2
4x10-5
6x10-8
9x10-11
background
Willacy et al. 1998
4x10-3
10-5
10-8
3x10-10
background

Figure 1

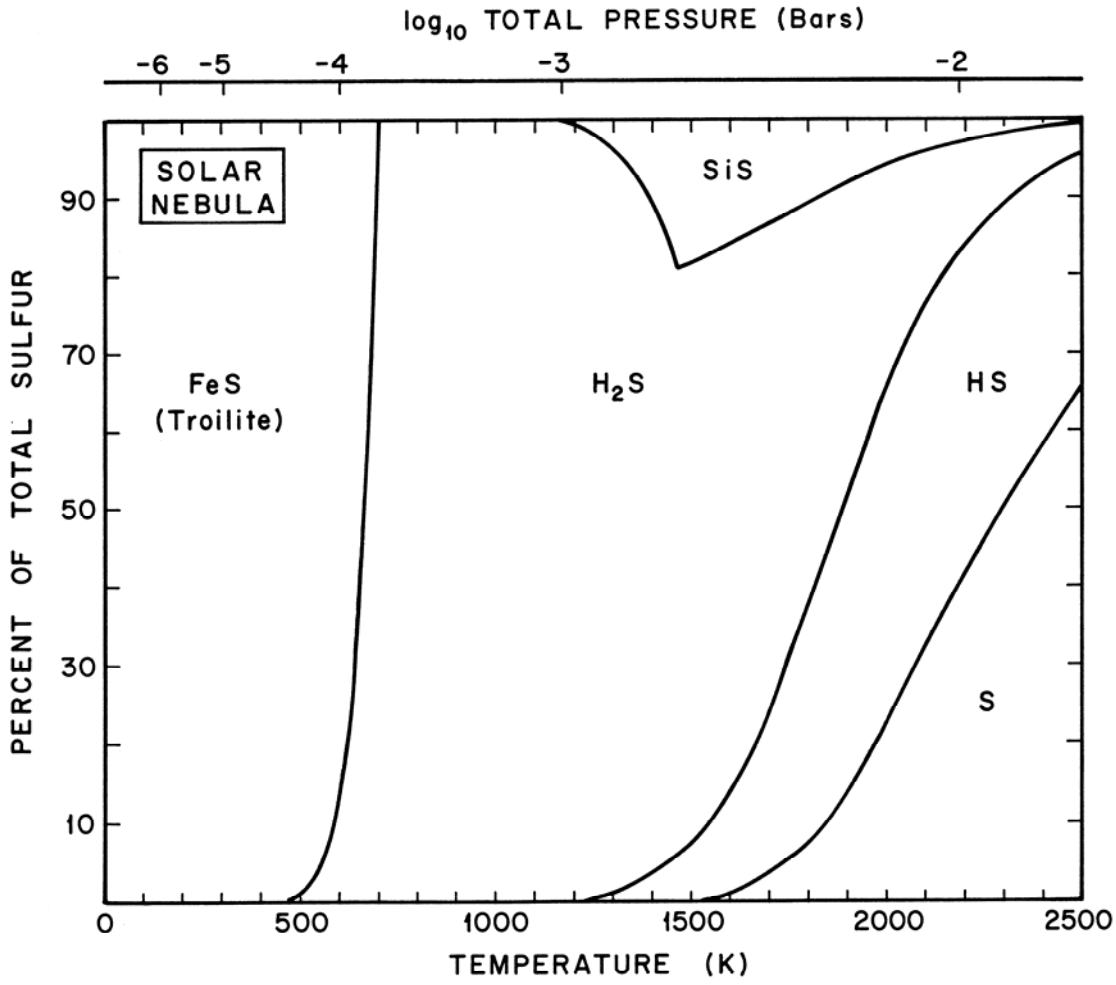
log10 TOTAL PRESSURE (Bars)
-6
-5
-4
-3
-2
SOLAR NEBULA
SiS
FeS (Troilite)
H2S
HS
S
PERCENT OF TOTAL SULFUR
90
70
50
30
10
0
500
1000
1500
2000
2500
TEMPERATURE (K)

Figure 2.

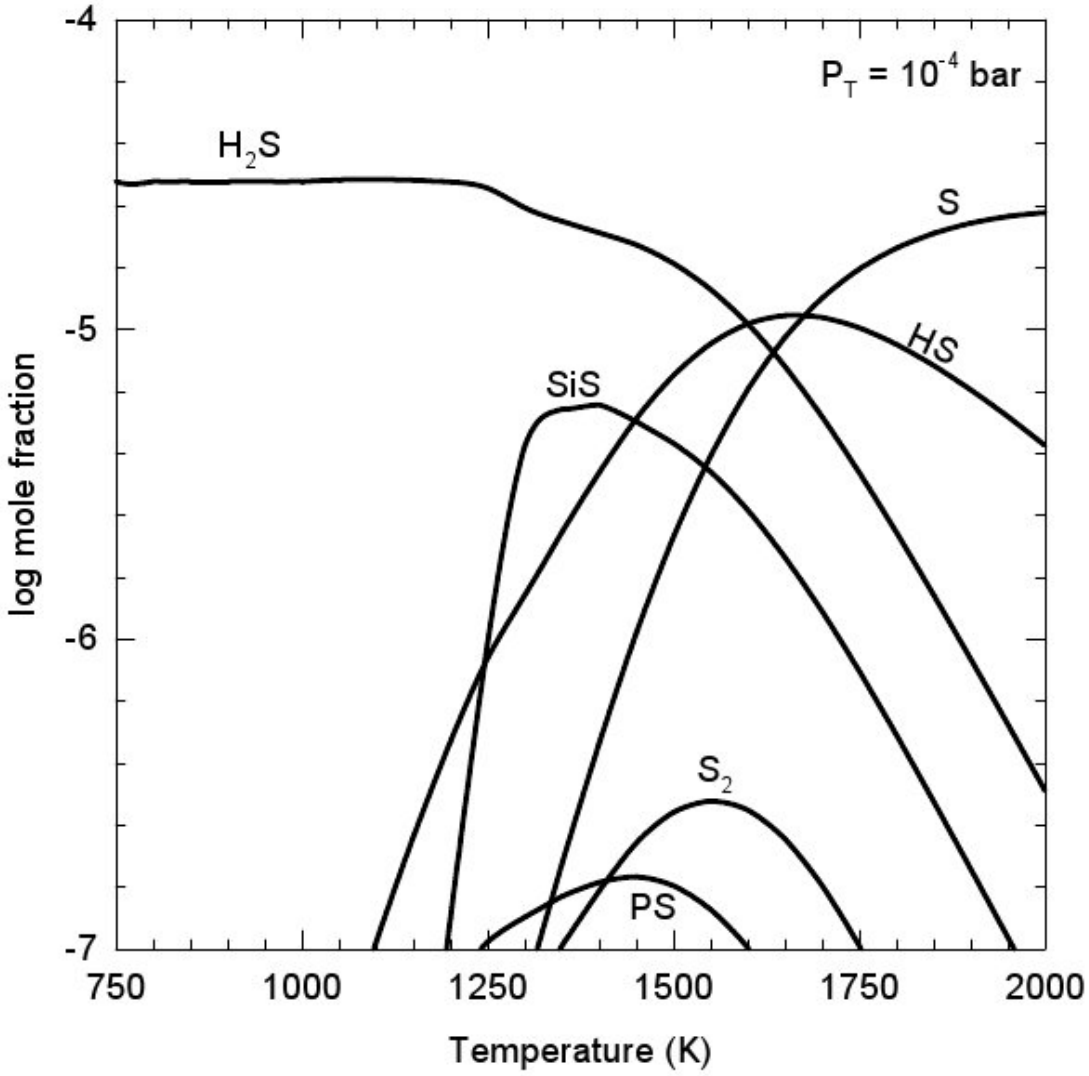

Figure 3. Sulfur chemistry

Figure 3

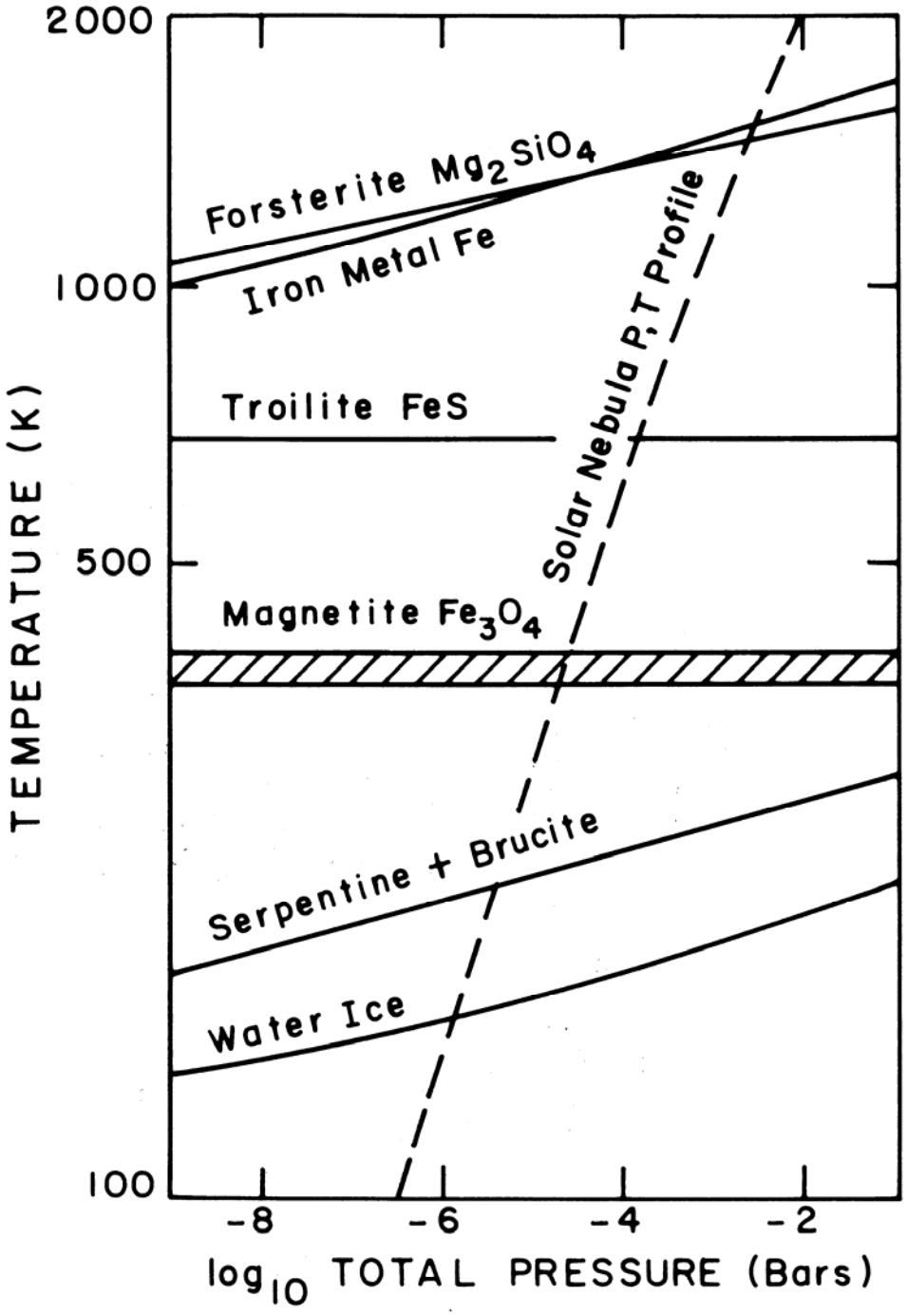
2000
1000
500
100
TEMPERATURE (K)
Forsterite Mg_2SiO_4
Iron Metal Fe
Troilite FeS
Magnetite Fe_3O_4
Solar Nebula P,T Profile
Serpentine + Brucite
Water Ice
-8
-6
-4
-2
$\log_{10}$ TOTAL PRESSURE (Bars)

Figure 4.

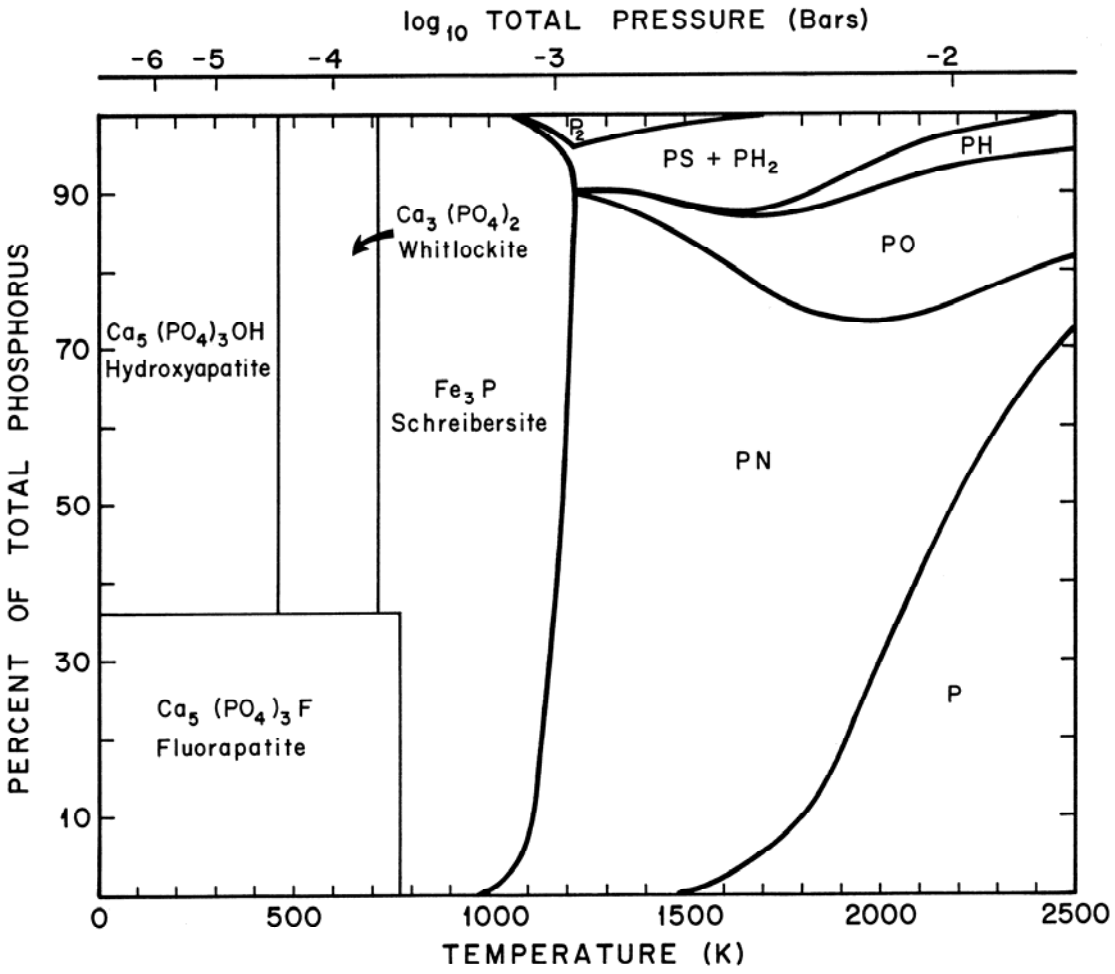
log 10 TOTAL PRESSURE (Bars)
-6
-5
-4
-3
-2
PERCENT OF TOTAL PHOSPHORUS
90
70
50
30
10
0
500
1000
1500
2000
2500
TEMPERATURE (K)
P2
PS + PH2
PH
PO
Ca3 (PO4)2
Whitlockite
Ca5 (PO4)3OH
Hydroxyapatite
Fe3P
Schreibersite
PN
P
Ca5 (PO4)3F
Fluorapatite

Figure 5.

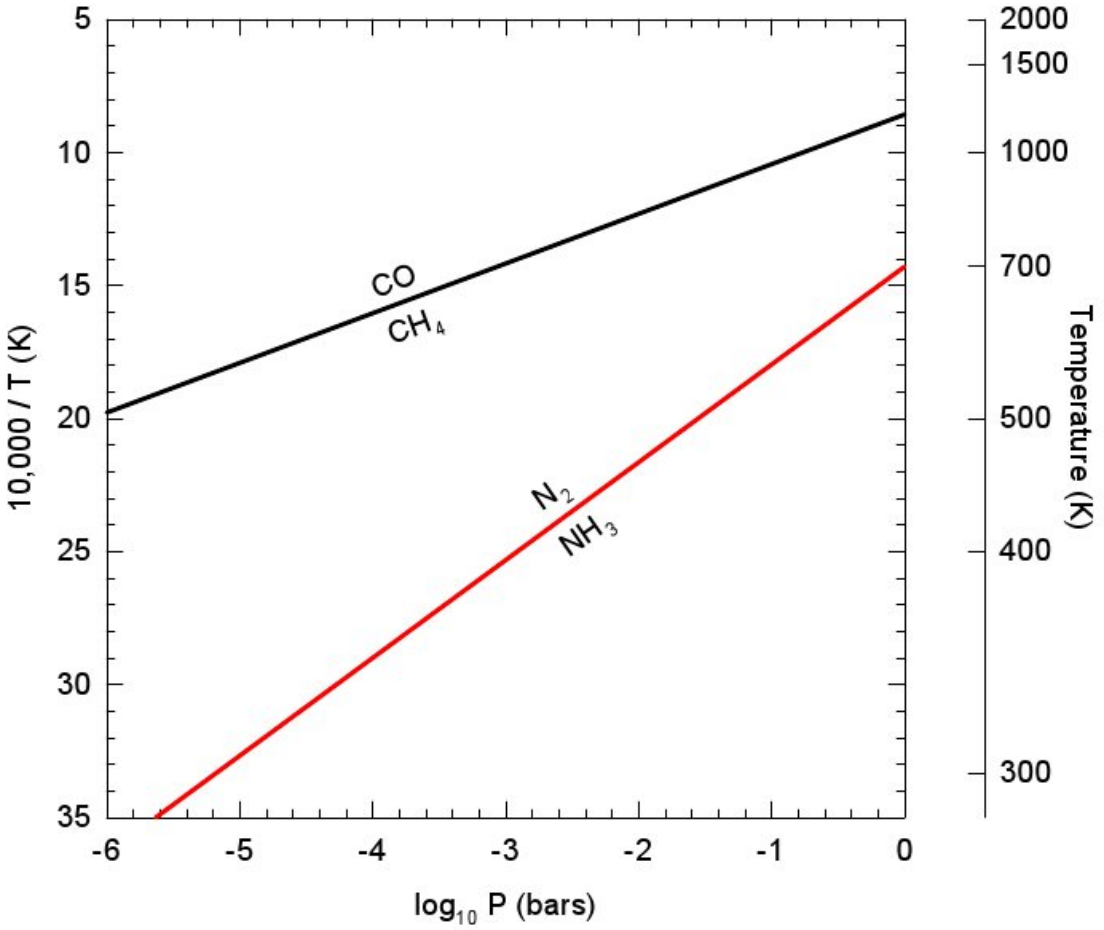

Figure 6. Carbon and Nitrogen ratios

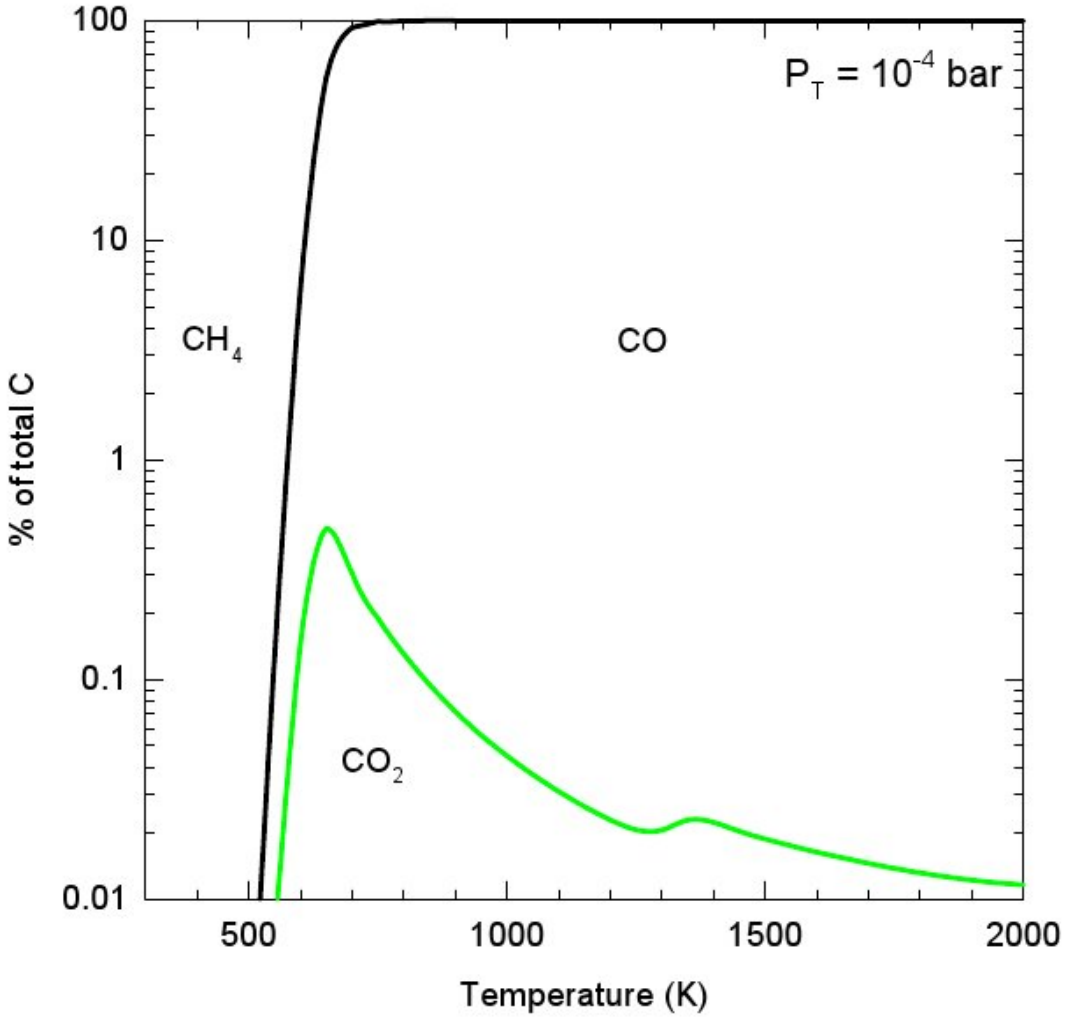

Figure 7. Carbon chemistry by element %.

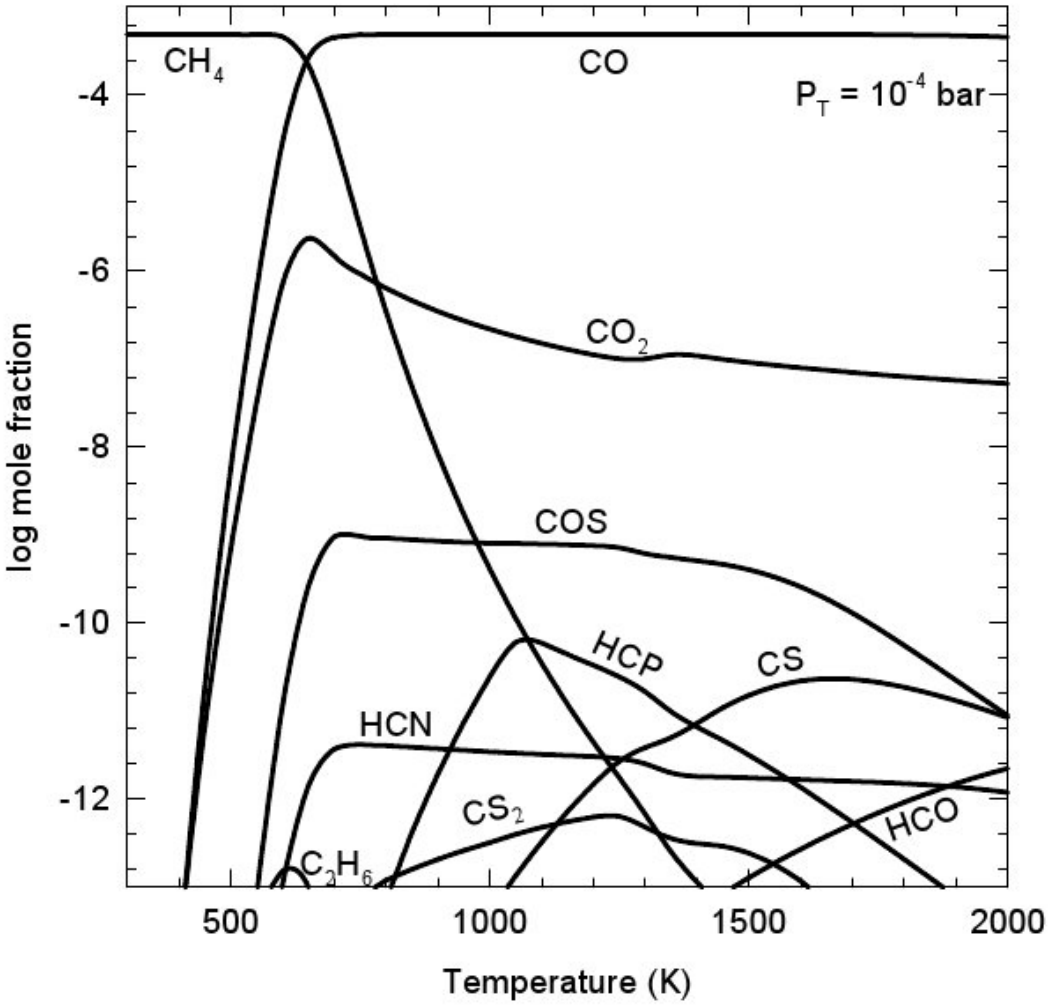

Figure 8. Carbon chemistry by mole fraction.

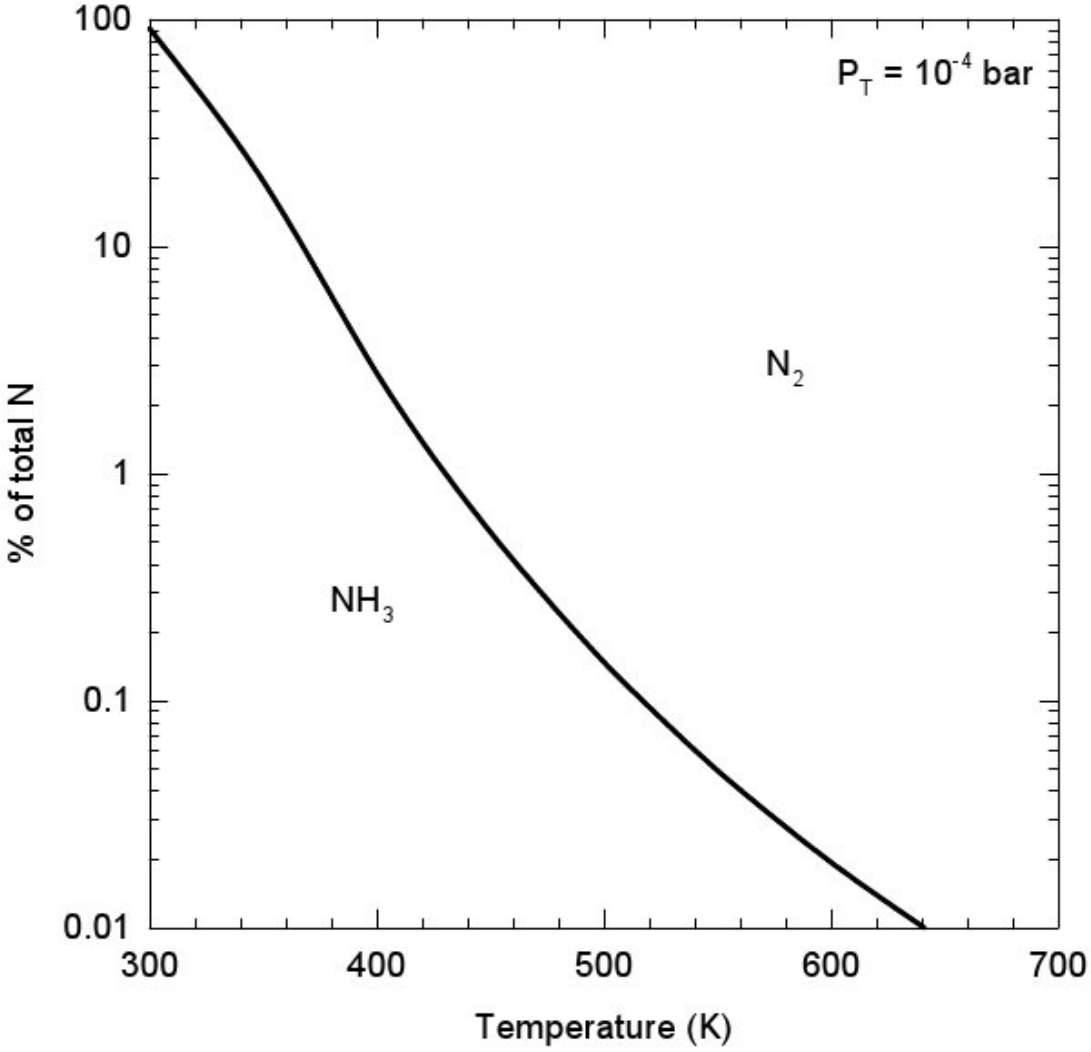

Figure 9. Nitrogen chemistry by element %.

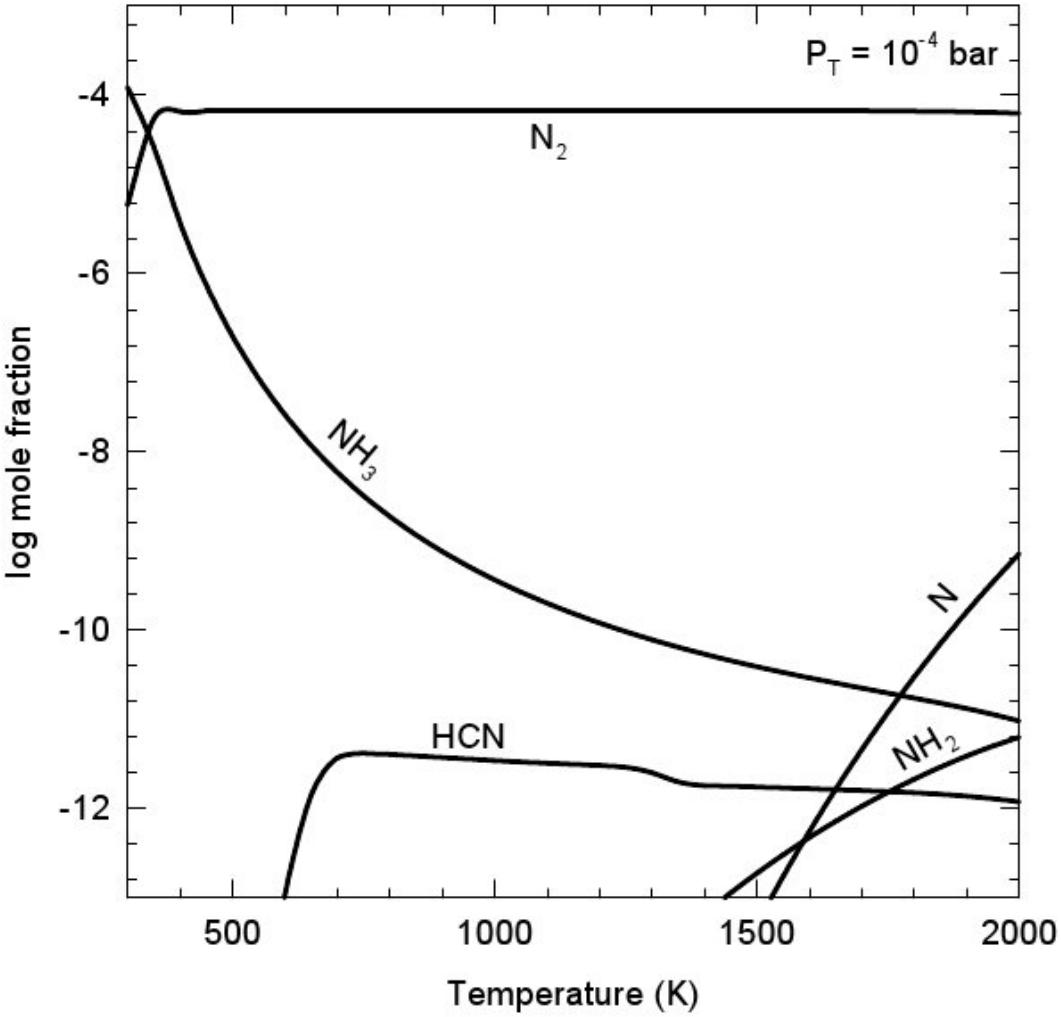

Figure 10. Nitrogen chemistry in mole fractions

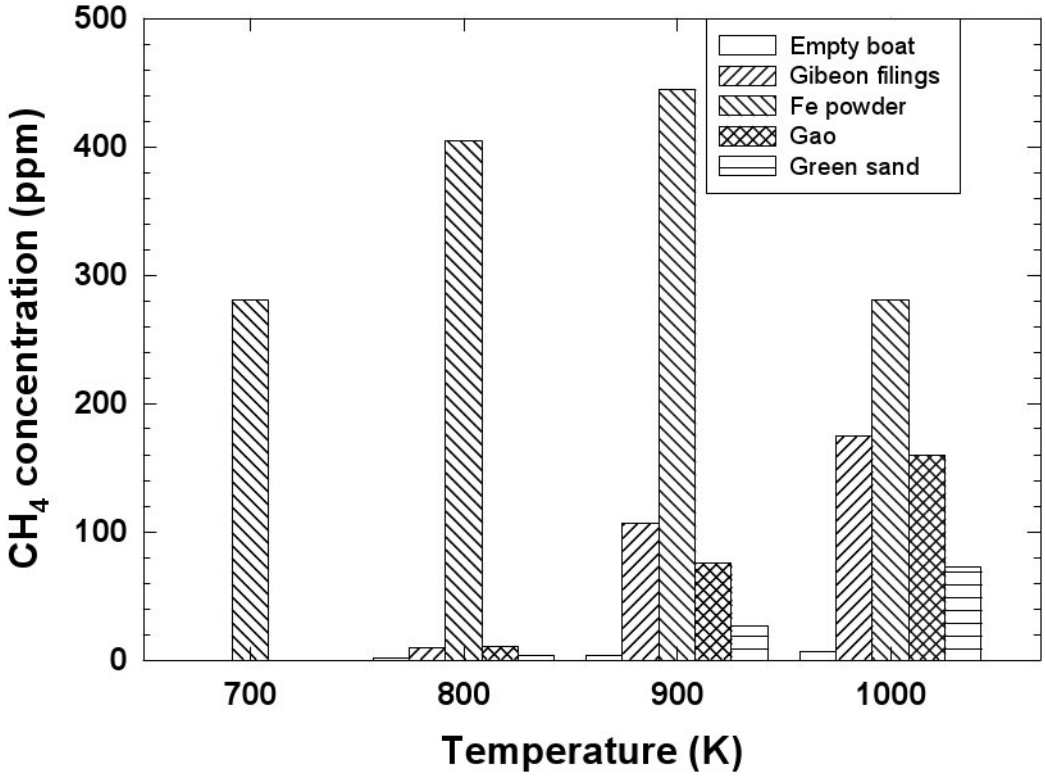
500
400
300
200
100
0
CH_4 concentration (ppm)
700
800
900
1000
Temperature (K)
Empty boat
Gibeon filings
Fe powder
Gao
Green sand

Figure 11.

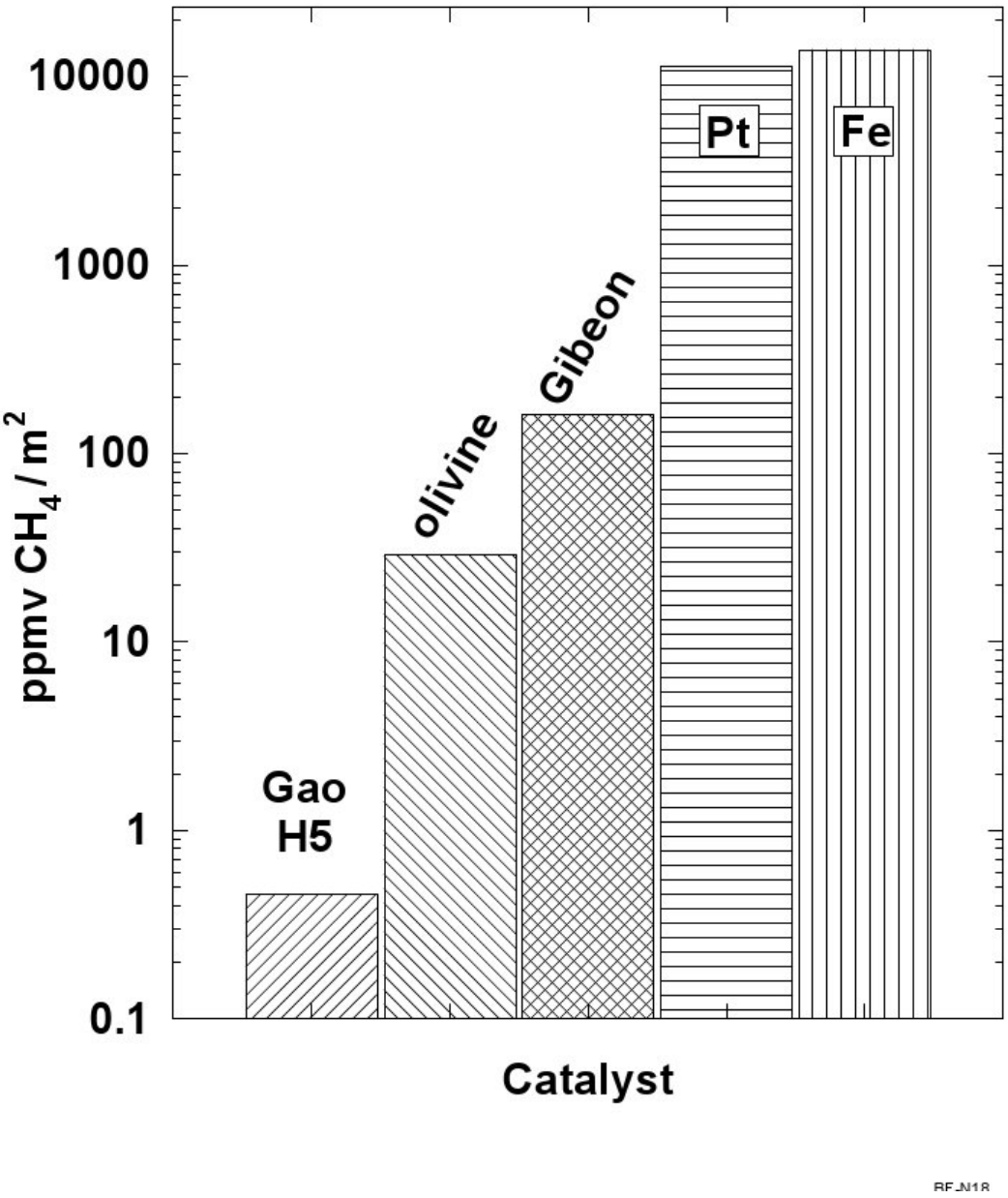
10000
1000
100
10
1
0.1
ppmv CH_4 / m^2
Gao
H5
olivine
Gibeon
Pt
Fe
Catalyst

Figure 12.

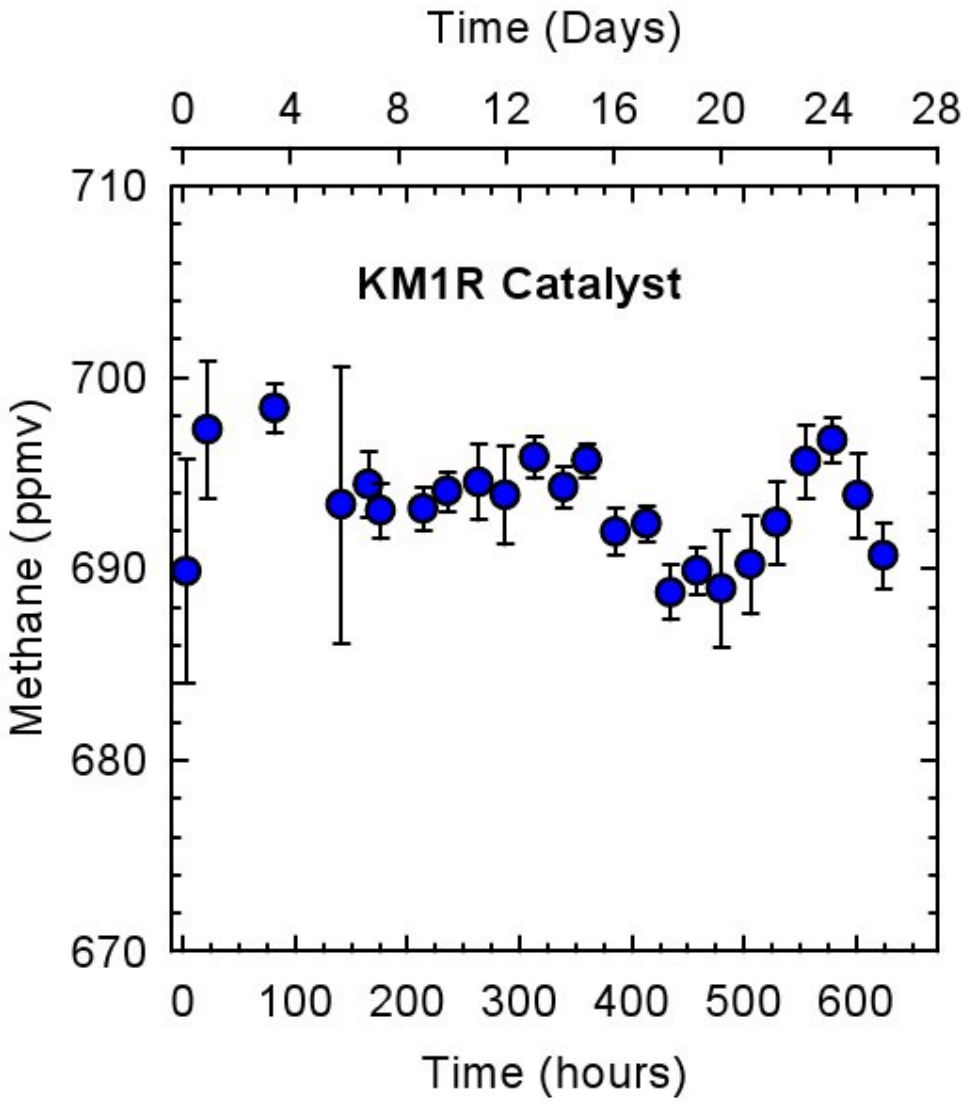
Time (Days)
0
4
8
12
16
20
24
28
KM1R Catalyst
Methane (ppmv)
710
700
690
680
670
0
100
200
300
400
500
600
Time (hours)

Figure 13.

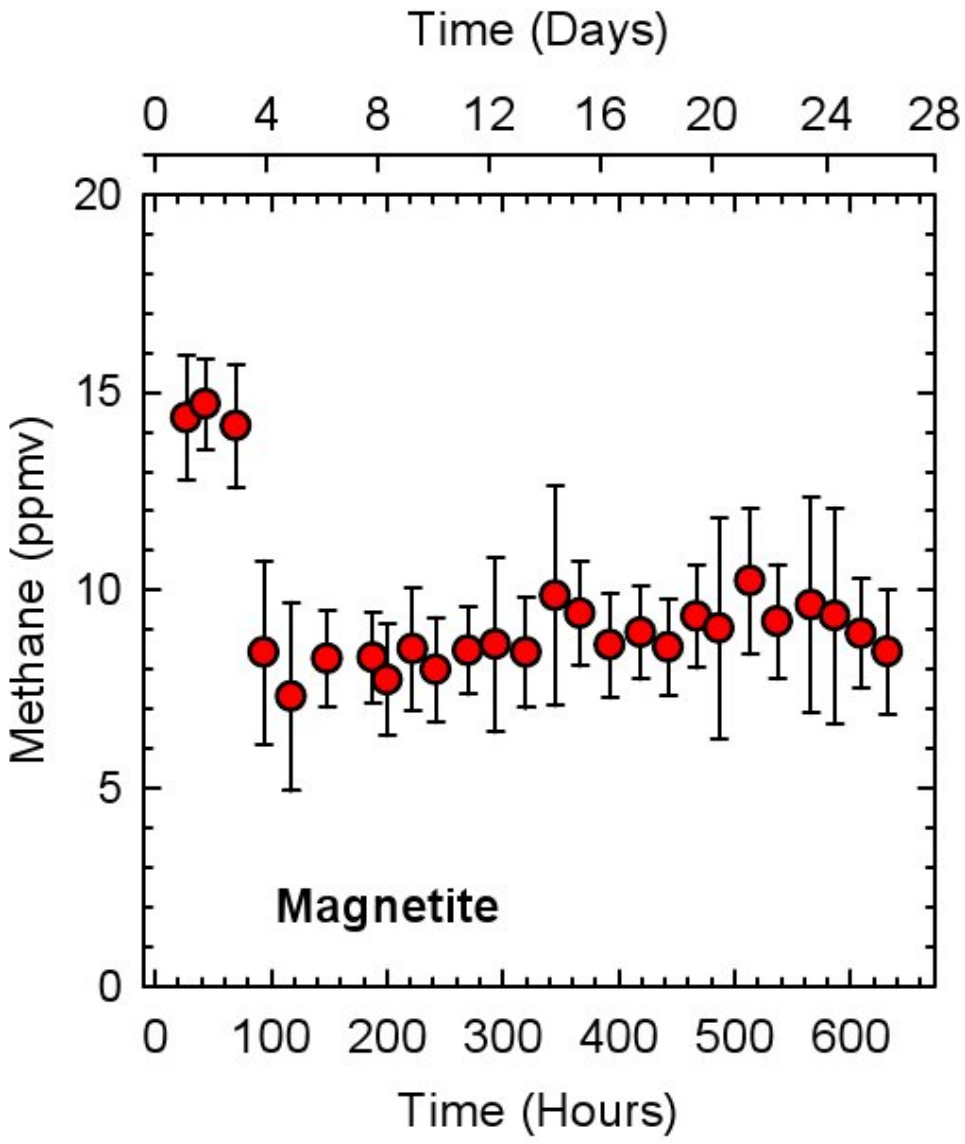
Time (Days)
0
4
8
12
16
20
24
28
20
15
10
5
0
Methane (ppmv)
Magnetite
0
100
200
300
400
500
600
Time (Hours)

Figure 14.